

Transformation of Ni-containing birnessite to tectomanganate: Influence and fate of weakly bound Ni(II) species

Zhongkuan Wu, Bruno Lanson, Xionghan Feng, Hui Yin, Zhangjie Qin, Xiaoming Wang, Wenfeng Tan, Zhongjun Chen, Wen Wen, Fan Liu

▶ **To cite this version:**

Zhongkuan Wu, Bruno Lanson, Xionghan Feng, Hui Yin, Zhangjie Qin, et al.. Transformation of Ni-containing birnessite to tectomanganate: Influence and fate of weakly bound Ni(II) species. Geochimica et Cosmochimica Acta, 2020, 271, pp.96-115. 10.1016/j.gca.2019.12.023 . insu-02984573

HAL Id: insu-02984573
https://insu.hal.science/insu-02984573

Submitted on 25 Nov 2020

HAL is a multi-disciplinary open access archive for the deposit and dissemination of scientific research documents, whether they are published or not. The documents may come from teaching and research institutions in France or abroad, or from public or private research centers.

L'archive ouverte pluridisciplinaire **HAL**, est destinée au dépôt et à la diffusion de documents scientifiques de niveau recherche, publiés ou non, émanant des établissements d'enseignement et de recherche français ou étrangers, des laboratoires publics ou privés.

*Manuscript

Transformation of Ni-containing birnessite to tectomanganate: Influence and fate of weakly bound Ni(II) species

Zhongkuan Wu[a,b], Bruno Lanson[b,*], Xionghan Feng[a], Hui Yin[a], Zhangjie Qin[a], Xiaoming Wang,[a] Wenfeng Tan[a], Zhongjun Chen[c], Wen Wen[d], Fan Liu[a,*]

[a] *Key Laboratory of Arable Land Conservation (Middle and Lower Reaches of Yangtse River) Ministry of Agriculture, College of Resources and Environment, Huazhong Agricultural University, Wuhan 430070, China*

[b] *Univ. Grenoble Alpes, Univ. Savoie Mont Blanc, CNRS, IRD, IFSTTAR, ISTerre, F-38000 Grenoble, France*

[c] *Beijing Synchrotron Radiation Facility, Institute of High Energy Physics, Chinese Academy of Sciences, Beijing 100039, China*

[d] *Shanghai Synchrotron Radiation Facility, Shanghai Advanced Research Institute Chinese Academy of Sciences, Shanghai 201204, China*

** Corresponding author: bruno.lanson@univ-grenoble-alpes.fr; liufan@mail.hzau.edu.cn*

Abstract

The geochemical behavior of nickel, an essential trace metal element, strongly depends on its interactions with Mn oxides. Interactions between the phyllomanganate birnessite and sorbed or structurally incorporated Ni have been extensively documented together with the fate of Ni along the transformation of these layered species to tunnel Mn oxides (tectomanganates). By contrast, interactions of phyllomanganates with weakly bound Ni species (hydrated Ni, Ni (hydr)oxides), that possibly prevail in natural Ni-rich (>10% NiO) manganates received little attention and the influence of these Ni species on the phyllomanganate-to-tectomanganate transformation remains essentially unknown. Within this framework, a set of phyllomanganate precursors with contrasting contents of Ni were prepared and subjected to a reflux process mimicking the natural phyllomanganate-to-tectomanganate conversion. Layered precursors and reflux products were characterized with a combination of diffractometric, spectroscopic, thermal, and chemical methods. Ni is essentially present as hydrated Ni(II) and Ni(II) (hydr)oxides in layered precursors with no detectable Ni sorbed at layer vacancy sites or structurally incorporated. Despite the high content (~1/3) of Jahn-Teller distorted Mn(III) octahedra in these layered precursors, which is known to be favorable to their conversion to tectomanganates, polymerization of $Ni(OH)_2$ in phyllomanganate interlayers is kinetically favored during reflux process. Asbolane, a phyllomanganate with an incomplete – island-like – octahedral layer of metal (hydr)oxides, is thus formed rather than todorokite, a common tectomanganate with a uniform 3×3 tunnel structure. A nitric acid treatment, aiming at the dissolution of the island-like interlayer $Ni(OH)_2$ layer, allows an easy and unambiguous differentiation between asbolane and todorokite, which is unaffected by the treatment. Both compounds exhibit indeed similar periodicities and can be confused when using X-ray diffraction, despite contrasting intensity ratios. $Ni(OH)_2$ polymerization hampers the formation of tectomanganates and likely contributes to the prevalence of phyllomanganates over

tectomanganates in natural environments. Most Ni is retained during the reflux process, part of Ni (~20%) being likely structurally incorporated in the reaction products, thus enhancing the sequestration of Ni in Mn oxides.

Keywords: nickel; buserite; asbolane; todorokite; Mn oxides

1. INTRODUCTION

Phyllomanganates and tectomanganates are the two mineral families accounting for most of Mn oxides found in terrestrial and aquatic environments (Post, 1999; Peacock and Sherman, 2007a). In the former, edge-sharing MnO_6 octahedra form layers whose symmetry depends on the abundance and distribution of Mn(III) octahedra, whereas in the latter, chains of edge-sharing $Mn(IV)O_6$ octahedra form the walls or floor/ceiling of tunnels. Birnessite is, together with its disordered structural analogue vernadite, the most common phyllomanganate and consists of a MnO_2 layer, whose layer charge deficit is compensated for by the presence of cations sorbed at layer vacancy sites or present as interlayer hydrated species (7.0-7.2 Å layer-to-layer distance). Heterovalent Mn cations and/or foreign transition metal cations can be hosted in both families, either structurally substituted for Mn(IV) or as charge compensating cations located in phyllomanganate interlayers or in tectomanganate tunnels (Post, 1999). The occurrence of natural phyllomanganates as micro- to nano-sized cryptocrystalline minerals usually enhances their surface reactivity that originates from their high negative layer charge and from the coexistence of heterovalent Mn cations in these structures. As the result, natural phyllomanganates are highly reactive with respect to both organic (Remucal and Ginder-Vogel, 2014) and inorganic compounds. Specifically, natural phyllomanganates are readily associated with transition metals such as Co, Cu, Zn, or Ni (Chukhrov, 1982; Manceau et al., 1987, 1992a,b, 2002, 2007a,b, 2014; Marcus et al., 2004; Bodeï et al., 2007; Peacock and Sherman, 2007a; Lanson et al., 2008; Spinks et al., 2017; Zawadzki et al., 2018), rare earth (Kasten et al., 1998; Ohta and Kawabe, 2001; Ohnuki et al., 2015; Zawadzki et al., 2018), and radioactive elements (Duff et al., 1999; Post, 1999).

In an effort to disentangle the mobility, (bio)availability, and fate of these elements in different geological settings, structural interactions of phyllomanganates with such foreign elements, and more especially with transition metals, have thus

attracted the attention of the scientific community over the last few decades (Manceau et al., 1997, 2002, 2014; Ohta and Kawabe, 2001; Lanson et al., 2002a; Marcus et al., 2004; Toner et al., 2006; Peacock and Sherman, 2007a,b; Peacock, 2009; Peña et al., 2010; Roque-Rosell et al., 2010; Sherman and Peacock, 2010; Yin et al., 2011a,b; Kwon et al., 2013; Yu et al., 2013; Burlet and Vanbrabant, 2015; Simanova et al., 2015). In most studies, foreign elements were structurally substituted for Mn(IV) in the MnO_6 octahedra or sorbed as inner-sphere complexes either at vacant layer sites and/or at particle edges (Manceau et al., 1997; Yin et al., 2011a, 2015; Yu et al., 2013; Ohnuki et al., 2015; Simanova and Pena, 2015; Qin et al., 2018). Similar to other transition metals, presence of Ni(II) forming inner-sphere complexes species at vacancy or edge sites and/or structurally incorporated in phyllomanganate layers has been extensively documented (Manceau et al., 2002, 2007a,b; Peacock and Sherman, 2007a,b; Grangeon et al., 2008; Peña et al., 2010; Yin et al., 2012, 2014; Kwon et al., 2013; Simanova et al., 2015). Under low pH conditions, Ni(II) occurs mainly as triple- or double-corner sharing (TCS and DCS, respectively) inner-sphere complex above/below vacancy or at edge sites of the phyllomanganate layers (Peacock and Sherman, 2007b; Grangeon et al., 2008; Peacock, 2009; Peña et al., 2010; Simanova et al., 2015). Migration from TCS/DCS sites to octahedral layer sites is favored by increasing contact time and increasing pH (Peacock, 2009), this structural incorporation within the octahedral MnO_2 layer being reversible (Peacock, 2009; Peña et al., 2010) and essentially restricted to low Ni contents (Manceau et al., 2002; Bodeï et al., 2007; Peacock and Sherman, 2007a,b; Kwon et al., 2013; Simanova et al., 2015; Atkins et al., 2016), consistent with natural occurrences (Manceau et al., 2002, 2007a,b; Bodeï et al., 2007; Peacock and Sherman, 2007a).

In addition, hydrated Ni(II) or Ni forming outer-sphere complexes (Turner and Buseck, 1981; Peacock and Sherman, 2007a) and Ni(II) (hydr)oxides (Chukhrov et al., 1987; Manceau et al., 1987, 1992a,b) may also be associated with Mn oxides. Despite their widespread natural occurrences for high Ni contents (NiO ~10-20 wt.%, – Llorca, 1988; Roque-Rosell et al., 2010; Ploquin et al., 2018), these weaker associations have received little attention compared to structurally incorporated Ni or to Ni inner-sphere

complexes. The presence of hydrated Ni(II) species in phyllomanganate interlayers leads to the presence of two planes of interlayer water molecules, thus increasing the layer-to-layer distance from ~7.2 Å (birnessite or vernadite) to ~9.6-10.2 Å (buserite – Burns et al., 1983; Chukhrov et al., 1987; Golden et al., 1987; Manceau et al., 1997, 2014; Bodeï et al., 2007; Wegorzewski et al., 2015). Such increased hydration of Ni-rich phyllomanganates has for example been reported by Manceau et al. (2007b). The presence of hydrated Ni(II) in phyllomanganate interlayers has been described also as favorable to the transformation of phyllomanganate to tectomanganates upon hydrothermal treatment (Ching et al., 1999; Luo et al., 1999; Onda et al., 2007), similar to Mg(II) (Golden et al., 1986, 1987). In addition, Ni(II) (hydr)oxides may polymerize in phyllomanganate interlayers either as a complete or as an incomplete brucite-like octahedral layer, leading to litiophorite- or asbolane-like species, respectively, both having a layer-to-layer distance of 9.4-9.8 Å (Chukhrov et al., 1987; Manceau et al., 1987, 1992a,b; Feng et al., 2001).

The present article thus focuses on the association of these weakly bound Ni(II) species with phyllomanganates. Synthetic samples with contrasting Ni contents were prepared and characterized by X-ray diffraction, Fourier transform infrared spectroscopy, thermogravimetric analysis, X-ray photoelectron spectroscopy, extended X-ray absorption fine structure spectroscopy (Mn and Ni K-edges). In addition, phyllomanganate samples were hydrothermally treated and reaction products characterized to investigate the effect of Ni on the phyllomanganate-to-tectomanganate transformation (Golden et al., 1986; Shen et al., 1993; Feng et al., 2004, 2010; Atkins et al., 2014; Grangeon et al., 2014, 2015; Zhao et al., 2015) and the fate of weakly associated Ni(II) species during this transformation. The negative impact of Ni, when present at high content, on this transformation is contrasted with that of Co. Buserite-, litiophorite-, and asbolane-like phyllomanganates all have interplanar periodicities similar to those of todorokite, a common tectomanganate with a uniform 3×3 tunnel structure (Post and Bish, 1988), however, leading to their frequent confusion (Burns et al., 1983). Special care was thus paid to allow differentiating these species using nitric acid treatment (Wu et al.,

2019), Fourier transform infrared spectroscopy and anomalous X-ray diffraction. An optimum procedure allowing this differentiation is proposed.

2. MATERIALS AND METHODS

2.1. Synthesis of layered precursors and reflux products

Both initial layered precursors and reflux products described in the present study were prepared as in our previous work on their Co analogues (Wu et al., 2019). Briefly, layered precursors were prepared after Feng et al. (2004) and Song et al. (2010) by adding a concentrated NaOH solution into a Ni(II) + Mn(II) solution, prepared from their chloride salts. The resulting solution was then mixed and bubbled with oxygen gas for 5 h. Resulting black precipitates were washed and one half was dried for subsequent analyses. Initial Ni / (Ni + Mn) ratios were 0.00, 0.01, 0.05, 0.10, 0.15, and 0.20. Accordingly, initial layered samples were named Bir, NiB1, NiB5, NiB10, NiB15 and NiB20, and those Ni-containing samples are collectively referred to as NiB. The other half of the precipitates was used to prepare todorokite through a reflux process following the protocol of Feng et al. (2004). Wet precipitates were thus exchanged with Mg^{2+}, rinsed, re-suspended in deionized water, and finally refluxed at 100 °C for 24 h. Reflux products were finally filtered, washed, and dried. Transformation products of Bir, NiB1, NiB5, NiB10, NiB15 and NiB20 are named Tod, NiT1, NiT5, NiT10, NiT15 and NiT20, respectively; they are collectively referred to as NiT except for Tod. Both layered precursors and reflux products were dried at 60 °C for three days and ground into fine powders.

2.2. Characterization of layered precursors and reflux products

The elemental composition of all samples was determined in triplicate using atomic absorption spectrometry (Varian AAS 240FS) from 0.1000 g of sample

dissolved in 25 mL solution of 0.25 mol L^{-1} $NH_2OH{\cdot}HCl$ and 5 mL of 1 mol L^{-1} H_2SO_4. In addition, the specific surface area (SSA) of the reflux products was determined with the Brunauer–Emmett–Teller (BET) method and a standard adsorption analyzer (Quantachrome Autosorb-1, JEDL-6390/LV). Finally, a non-reducing nitric acid treatment (Wu et al., 2019) was performed to differentiate tectomanganates (todorokite) from phyllomanganates (buserite-, lithiophorite-, or asbolane-like phases – Wu et al., 2019). Briefly, 0.1 g sample was put in 250 mL of a 1 M HNO_3 solution with soft stirring at ambient temperature (20 °C). At different time intervals, 5 mL of the suspension was collected and readily filtered through a 0.22 µm membrane to determine Mn, Ni, and Mg release. After 1 week of this HNO_3 treatment, residual samples were dried at 60 °C for 3 days and analyzed with X-ray diffraction (XRD) at a scan speed of l0 ° 2θ.min^{-1}.

Mineralogy of all samples was determined from powder XRD analysis using a Bruker D8 Advance diffractometer equipped with Cu Kα source (λ = 0.15418 nm) and operated at 40 kV and 40 mA. XRD patterns were collected at 0.02 °2θ intervals using a continuous scan mode. XRD data was collected on fresh samples (dried at 60 °C for three days) at a scan speed of l0 ° 2θ.min^{-1}. To assess the stability of their hydration, XRD data was collected on fresh samples after heating to 140 °C. Finally, XRD patterns were collected at l ° 2θ.min^{-1} for aged samples that were kept dry in the dark for three months. Synchrotron XRD patterns were also collected on selected reflux products on beamline BL14B1 at the Shanghai Synchrotron Radiation Facility (SSRF) and on beamline 4B9A at the Beijing Synchrotron Radiation Facility (BSRF). At BSRF, XRD data was collected at the Mn K-edge (6.5 keV), Ni K-edge (8.3 keV), and 12 keV with a typical beam size of 2 × 1 mm^2, whereas the 18 keV data was collected at SSRF with a typical beam size of ~0.2 × 0.3 mm^2. In both cases, X-rays were monochromatized with a double-crystal Si (111) monochromator. Finally, high-energy X-ray scattering data was collected in transmission mode on beamline 11-ID-B at the Advanced Photon Source (Argonne National Laboratory, Argonne, IL), using a ~90 keV X-ray energy. Pair distribution functions (PDF) and differential PDFs were calculated as described elsewhere (Li et al., 2011; Wang et al., 2013).

Infrared spectra were collected for both layered precursors and reflux products using a Bruker VERTEX 70. For each sample, 64 spectra were collected and summed over the 4000–400 cm^{-1} range with a 4 cm^{-1} resolution (Zhao et al., 2015). Micromorphology of the reflux products and lattice periodicities were observed a Jeol JEM2100F transmission electron microscope (TEM) operated at 200 kV. TGA was performed on a NETZSCH TG 209 instrument with a heating rate of 10 °C min^{-1} and a N_2 flow of 20 mL min^{-1}. Finally, X-ray photoelectron O1s spectra were collected with a VG Multilab2000. X-ray photoelectron spectroscopy (XPS) measurements used an Al Kα X-ray source (1486.6 eV) at a chamber base pressure of 3×10^{-9} Torr (Yin et al., 2011a). The O 1s spectra were collected with a 25 eV pass energy and 0.1 eV energy steps, and analyzed with the Avantage software. All samples were charge-corrected to C 1s with a binding energy of 284.80 eV collected from the surface adventitious carbon (Wang et al., 2010). A Shirley-type background was subtracted before deconvolution and fitting. A Lorentzian:Gaussian ratio of 30:70 was used for all the fittings.

Finally, X-ray absorption spectra were collected at the Mn and Ni K-edges on the 1W1B beamline of BSRF to determine the relative proportions of Mn(II), Mn(III), and Mn(IV) species and the local environments of Mn and Ni in both layered precursors and reflux products. Data was recorded at room temperature in transmission (Mn) and fluorescence (Ni) modes, and the energy was calibrated using metallic Mn/Ni foils as references. Extended X-ray absorption fine structure (EXAFS) spectra were processed using Athena and Artemis (Ravel and Newville, 2005). X-ray absorption near-edge structure (XANES) spectra of both layered precursors and reflux products were used to determine Mn average oxidation state (AOS) with a specific linear combination fitting method (the so-called Combo method). Mn(II), Mn(III), and Mn (IV) reference compounds were those of the original study (Table 1 in Manceau et al., 2012).

3. RESULTS

3.1. Elemental composition

With increasing Ni content, the Mn content decreases from ~55.4 to ~44.8 wt.% for layered precursors and from ~54.4 to ~49.2 wt. % for reflux products (Table 1). The Ni/(Mn+Ni) molar ratios are essentially similar in layered precursors and their respective reflux products, with only a very limited fraction of Ni being lost either during the Mg-for-(Na,Ni) exchange or during the subsequent transformation process. In addition, the Mg wt.% in the reflux products significantly decreases from ~3.95 wt.% in the Ni-free Tod sample to ~2.11 wt.% in NiT20, thus suggesting a competition between Mg and Ni for interlayer and/or tunnel sites of layered precursors and/or of reflux products. Specific surface area (SSA) of NiT samples, as measured with the BET method, is systematically higher than that of Ni-free Tod, but no systematic evolution of SSA is observed with the increase of Ni content.

3.2. Powder X-ray diffraction

X-ray diffraction (XRD) patterns collected on fresh Bir (not shown) are essentially similar to those recorded after a few months of aging and display reflections at 7.2, 3.6, ~2.45, and ~1.42 Å, typical for birnessite (Drits et al., 1997; Lanson et al., 2002b). Similar reflections are observed for fresh NiB5 and NiB10 samples (Fig. S1), in addition to a broad maximum peaking at ~4.6 Å. The intensity of this maximum increases with increasing Ni concentration in the initial solution and is thus likely related to the presence of Ni (hydr)oxide (ICDD #13-0229), whose formation was reported under similar experimental conditions (oxidation of a Ni-rich alkaline solution – Feitknecht et al., 1956). Consistently, the intensity of this maximum is increased further for NiB15 and NiB20. These two samples exhibit also reflections at ~2.45, and ~1.42 Å, typical for layered manganates, the basal reflections

of which indicate a 9.9-10.0 Å layer-to-layer distance (Fig. S1). Upon moderate heating (140 °C), these reflections shift to indicate a 7.2 Å layer-to-layer distance typical for birnessite, as the result of interlayer cation partial dehydration (Golden et al., 1986; Manceau et al., 1987; Drits et al., 1997). The initial presence of two planes of interlayer H_2O molecules in NiB15 and NiB20 (buserite) is most likely indicative of the presence of interlayer hydrated Ni(II) cations, whose hydration is reduced upon heating. Sample heating also results in a decrease of the intensity of the ~4.6 Å maximum.

After aging for about three months, all layered precursors but NiB20 display over the low-angle region (5-30 °2θ) strong basal reflections at ~7.2 and ~3.6 Å typical for birnessite and indicative of the spontaneous dehydration of NiB15 interlayers (Fig. 1). Two planes of H_2O molecules are still present in most NiB20 interlayers (buserite), however. Splitting of reflections at ~2.45 and ~1.42 Å, and more generally positions of the reflections over the high-angle region (30-85 °2θ – Fig. 1), unambiguously indicate that initial Bir is a triclinic birnessite (ICDD #43-1456), consistent with the synthesis protocol (Lanson et al., 2002b). With increasing Ni content, high-angle reflections broaden significantly thus indicating a decrease in the coherent scattering domain size. In addition, the resolution of these reflections decreases also with increasing Ni content, suggesting a minor increase of layer symmetry from orthogonal ($a > b\sqrt{3}$, $\gamma = 90°$) to hexagonal ($a = b\sqrt{3}$, $\gamma = 90°$ – Yin et al., 2015). Positions of birnessite *hkl* reflections remain essentially unchanged, however, indicative of the persistence of the orthogonal layer symmetry in Ni-rich layered precursors. The broad maximum at ~4.6 Å is present also in aged samples.

Reflux products systematically show reflections at ~9.6 Å, ~4.8 Å, ~3.2 Å, ~2.46 Å, ~2.39 Å, ~2.22 Å, ~1.95 Å, ~1.73 Å, ~1.52 Å, and ~1.42-1.41 Å, that are typical of todorokite (ICDD #38-0475 – Atkins et al., 2014, 2016). For the Ni-free Tod, relative intensity of the three low-angle reflections (at ~9.6, ~4.8, and ~3.2 Å) decreases in the order $I_{9.6} > I_{4.8} >> I_{3.2}$, consistent with relative intensities of todorokite 001/100, 002/200, and 003/300 reflections (Post et al., 2003), respectively. With increasing Ni content, the positions of both ~9.6 and ~4.8 Å reflections shift

towards higher angles for NiT15 and NiT20, compared to Ni-free Tod (Fig. S2) and the ~4.8 Å reflection becomes predominant, consistent with previous reports of todorokite prepared in the presence of various divalent metals (Shen et al., 1993, 1994; Ching et al., 1999; Nicolas-Tolentino et al., 1999; Fuertes et al., 2012) and asymmetric. Although not described as such in these references, this intensity ratio modification is consistent with the presence of asbolane, a phyllomanganate with an incomplete – island-like – octahedral layer of metal (hydr)oxides in the interlayer (Chukhrov et al., 1987; Golden et al., 1987; Fan and Gerson, 2015). The presence of these incomplete brucite-like octahedral layers between MnO_2 layers precludes the collapse of the layer-to-layer distance to ~7.2 Å upon heating (Fig. S3)

3.3. Anomalous XRD patterns

To investigate further the possible origin of the observed contrasting $I_{4.8}/I_{9.6}$ intensity ratios, XRD patterns of Tod, NiT15, and NiT20 were recorded at different energies, including Mn and Ni K-edges to modify the contribution of these elements to the structure factor (F_{hkl}). These XRD patterns logically exhibit reflections at similar d-values (Fig. 2a-d). Except for the pattern recorded at the Mn K-edge all Tod patterns also display similar low $I_{4.8}/I_{9.6}$ intensity ratios (Fig. S4), consistent with previous reports (Shen et al., 2011). Contrastingly, the $I_{4.8}/I_{9.6}$ intensity ratio is significantly higher for NiT15 and NiT20 compared to Tod, and varies significantly for these two samples as a function of the energy used for data collection. Specifically, NiT15 and NiT20 display highest $I_{4.8}/I_{9.6}$ intensity ratios at the Mn K-edge and lowest ratios at the Ni K-edge, whereas similar ratios are obtained for XRD patterns recorded at energies different from the two absorption edges (Figs. 2a-d; S4). Both features indicate contrasting structures of Tod and Ni-rich NiT products depending on the initial Ni content.

As reported in the early descriptions of asbolane, this compound exhibits high values of the $I_{4.8}/I_{9.6}$ intensity ratio (Chukhrov, 1982; Llorca, 1988; Fan and Gerson, 2015), consistent with XRD patterns calculated for such a structure hosting an

incomplete $Ni(OH)_2$ layer sandwiched in between two MnO_2 layers (Fig. 2e). In addition, for a given composition, this ratio increases when the contribution of Mn atoms to the structure factor is reduced (XRD data recorded at the Mn K-edge – Fig. 2a) and decreases when the contribution of Ni atoms to the structure factor is reduced (XRD data recorded at the Ni K-edge – Fig. 2b), consistent with the data. In addition, this ratio increases with the completeness of interlayer plane (Fig. 2e). Together with the collapse of layer-to-layer distance upon acid-dissolution of the incomplete $Ni(OH)_2$ layer (see below), these variations of the $I_{4.8}/I_{9.6}$ intensity ratio can be ascribed to the presence of asbolane, rather than todorokite, in the reflux products.

3.4. FTIR

FTIR spectra of todorokite and of other 3×n tectomanganates display a band at ~760 cm^{-1}, typical for the corner-sharing linkage in their structures (Fig. 3 – Golden et al., 1986; Feng et al., 2004; Julien et al., 2004; Atkins et al., 2014; Zhao et al., 2015). This band is clearly visible in Tod FTIR spectrum but steadily decreases in intensity with increasing Ni content, most likely as the result of the decreasing proportion of 3×n tectomanganates in Ni-rich reflux products. Consistent with their layered structure, this band is absent in FTIR spectra of layered precursors. Rather, two lines at ~820 and ~950 cm^{-1} are visible in the FTIR spectra of Ni-containing layered precursors. These two lines are visible also in the spectra of related reflux products, although their intensity is reduced after the reflux treatment. The peak at ~820 cm^{-1} visible in NiB and NiT was identified as a combination lattice mode band in Ni (hydr)oxides (Hall et al., 2015), which is consistent with the XRD analysis.

3.5. HRTEM

Consistent with previous studies (Turner and Buseck, 1981; Golden et al., 1986; Shen et al., 1993; Feng et al., 2004; Wu et al., 2019), crystals with fibrous and plate-like morphologies are systematically present in the reflux products (Fig. 4), the

former dominating in Tod and NiT1 (Figs. 4a-c), whereas platy crystals dominate samples having higher Ni-contents (NiT5 and NiT15; Figs. 4f, i). Fiber-shaped crystals (Figs. 4 e, g, h) often display lattice fringes with a typical ~1 nm periodicity, corresponding to the 3×3 todorokite tunnel structure (Golden et al., 1986; Feng et al., 2004). As it is common in todorokite, fibers are often aligned at ±120° with respect to each other, thus forming trilling patterns (Siegel and Turner, 1983; Golden et al., 1986; Feng et al., 2004; Bodeï et al., 2007; Xu et al., 2010; Atkins et al., 2014). Visible lattice fringes in the plates are commonly more diverse than in the fibers (Figs. 4 b, d and j), typical for ***a***-disordered todorokite (Xu et al., 2010; Wu et al., 2019). Lattice fringes are also visible in short rods and small plates, indicating the initial development of tunnel structure therein (Figs. 4 g, h – Golden et al., 1986). Finally, smooth surfaces without visible fringes, that are most likely typical for phyllomanganate crystals (Golden et al., 1986, 1987; Wu et al., 2019), are also visible (Figs. 4 g – zone 4, 4i, j – zone 1, 4k – zone 5). Interestingly, some platy particles exhibit lattice fringes over specific zones with smooth surfaces (Figs. 4g, j). This dual character is possibly related to the initial development of tunnel structures in specific zones of the particles whereas other zones maintain their initial planar structure (Golden et al., 1987; Wu et al., 2019).

3.6. Nitric acid treatment

Upon equilibration in nitric acid, Mn release from layered precursors reaches equilibrium within 12 hrs, the proportion of Mn released from NiB is higher than that released from Bir, (Fig. 5a), possibly as an effect of reduced crystal size. For reflux products, the release of Mn is slower, reaching equilibrium after ~48 hrs, and is essentially the same for all NiT samples (Fig. 5b), except for NiT5. Ni release is much slower than that of Mn, reaching a plateau after ~168 hrs in both layered precursors (Fig. 5c) and reflux products (Fig. 5d). The proportion of Ni released differs however in the two series of samples as essentially all Ni is released from layered precursors whereas ~20% of Ni remains in the reflux products, possibly indicative of Ni

structural incorporation. Finally, Mg is systematically totally released from reflux products, possibly at a slower rate with increasing Ni content (Fig. 5f).

After acid treatment, the XRD pattern of Tod is essentially alike that of the initial reflux product and typical for todorokite (Fig. 5e). On the other hand, XRD patterns recorded on NiT15 and NiT20 after acid treatment exhibit, over the low-angle region, peaks at ~7.2 and ~3.6 Å, typical for the phyllomanganate birnessite, rather than peaks at ~9.6, ~4.8, and ~3.2 Å, as expected for todorokite (Fig. 5e). These two XRD patterns are actually similar to the one recorded on Bir after acid treatment and match XRD pattern of hexagonal birnessite (ICDD #23-1239), which was obtained from the low-pH equilibration of an initial triclinic birnessite (Lanson et al., 2000). The evolution of XRD patterns recorded from reflux products upon acid treatment is consistent with that observed for an asbolane-like phyllomanganate (Wu et al., 2019). The structure of these ~9.6 Å phyllomanganates consists of an octahedral MnO_2 layer similar to that of birnessite, with an incomplete octahedral $Me(OH)_2$, MeOOH, or MeO_2 sheet, possibly incommensurate with the MnO_2 layer, in the interlayer (Chukhrov, 1982; Manceau et al., 1987; Fan and Gerson, 2015). This incomplete interlayer octahedral sheet is solubilized by the acid treatment leading to the observed 7.2 Å layer-to-layer distance (Wu et al., 2019). Such a peak at ~7.2 Å is visible in the XRD pattern of acid-treated NiT5 and NiT10, and its intensity increases with increasing Ni content, becoming the sole visible diffraction signature in acid-treated NiT15 and NiT20 (Fig. 5e).

3.7. Thermogravimetric analysis

Thermogravimetric analyses of layered precursors systematically show a significant weight loss at 140-150 °C corresponding to the dehydration of interlayer Na^+ and Ni^{2+} cations, this weight loss decreasing with increasing Ni content (Figs. 6a, c; Table 2). A minor weight loss (2.4-2.9% in Bir, NiB5, NiB10, and NiB15) is also observed for these samples below 100 °C, which is most likely related to the departure of adsorbed water (Gaillot et al., 2003). This low-temperature weight loss is

significantly increased for NiB20 (9.25%), however, most likely as the result of a low-temperature buserite-to-birnessite transition associated with the loss of one plane of interlayer H_2O molecules as observed during moderate heating of fresh NiB samples (Fig. S1). A significant weight loss (4.10 and 6.72% for NiB5 and NiB20, respectively) is observed also for NiB samples over the 170-400 °C range. This weight loss is essentially absent in the TGA curve of Bir (1.78%) and increases with Ni content. It is likely related to the presence of the Ni (hydr)oxide responsible for the broad XRD maximum peaking at ~4.6 Å (Fig. 1). Finally, a weight loss is observed at ~550 °C for all layered precursors, with no significant influence of the Ni content, probably indicating the reduction of MnO_2 to Mn_2O_3 (Bish and Post, 1989).

TGA curves recorded for reflux products significantly differ from those of their layered precursors, with weight losses at ~150, ~285, ~440, and ~545 °C for Tod (Figs. 6b, d). The weight loss observed from ~110-240 °C is most likely related to the loss of the H_2O molecules hydrating cations present in todorokite tunnels (Bish and Post, 1989). With increasing Ni content, this weight loss decreases (from 8.05 to 6.12% in Tod and NiT20, respectively) and shifts towards lower temperatures, most likely indicative of the mineralogical evolution evidenced by XRD data recorded on acid-treated reflux products (Fig. 5e). For NiT10, this low-temperature weight loss splits in a doublet owing to the coexistence of todorokite and asbolane (Fig. 5e). The weight loss occurring at ~285 °C is also ascribed to the departure of tunnel water (Bish and Post, 1989). TGA curves obtained for Tod and NiT20 also differ significantly over this range, with a shift of the weight loss towards higher temperatures in NiT20 compared to Tod. Evolution with increasing Ni content, is not as systematic as that observed for the low-temperature weight loss, however (Fig. 6d). The third weight loss occurring at ~440 °C appears as a distinct signature for the presence of todorokite, as its intensity decreases with increasing Ni content to vanish for NiT15 and NiT20 which essentially contain asbolane (Fig. 5e). A last weight loss occurs at 520-550 °C, a temperature similar to that reported for layered precursors at ~550 °C (Figs. 6b, d).

3.8. O1s X-ray photoelectron spectroscopy

Consistent with the systematic prevalence of [MnO_6] building octahedral in both phyllomanganates and tectomanganates, all O1s XPS spectra are dominated by a peak at ~529.6 eV (Fig. 7), typical for oxygen (O^{2-}) in metal oxides. This main peak is asymmetric and displays a tail on its high-energy side for both layered precursors and reflux products. This tail at ~531-535 eV can be decomposed into the contributions of oxygen atoms from hydroxyl groups (OH^-; 530.9-531.6 eV) and from water molecules (532.2-533.4 eV). For layered precursors, the intensity of this tail, and more especially that of the OH^- contribution, increases with increasing Ni content (Fig. 7; Table S1), whereas the H_2O contribution is about constant for all NiB samples but NiB20 that shows a slightly higher proportion of O atoms from H_2O molecules, consistent with TGA data. In reflux products the contribution of O atoms in hydroxyl groups is significantly higher in NiT samples compared to Tod, consistent with the presence of asbolane-like phyllomanganate in Ni-rich reaction products. On the other hand, the H_2O contribution shows no systematic evolution with Ni content (Fig. 7; Table S1). Finally, relative intensities of peaks corresponding to OH^- and H_2O contributions are significantly increased in NiT samples compared to their corresponding layered precursors, at least under the deep vacuum conditions prevailing during the XPS measurements.

3.9. X-ray absorption spectroscopy

3.9.1. Mn K-edge XANES

Relative proportions of Mn(II), Mn(III), and Mn(IV) species and Mn average oxidation state (AOS) have been determined using the Combo method (Table 3 – Manceau et al., 2012). Results consistently indicate high (~1/3) relative proportions of Mn(III) in both layered precursors and reflux products, which is considered a key condition for the phyllomanganate-to-tectomanganate conversion (Cui et al., 2008; Atkins et al., 2014, 2016; Grangeon et al., 2014, 2015; Zhao et al., 2015; Li et al.,

2016). The measured proportion of Mn(III) is slightly lower in Ni-free samples compared to the Ni-bearing ones (Table 3) and no significant difference is observed between layered precursors and their reflux products. In all cases, the Mn(II) content is null within the experimental error.

3.9.2. Mn K-edge EXAFS

EXAFS spectra of both layered precursors and of reflux products show significant evolutions with increasing Ni content, thus indicating that the presence of Ni affects the local structure of manganates in the two series of samples (Fig. 8). The EXAFS spectrum collected for Ni-free layered precursor (Bir) is typical for triclinic birnessite over both the staircase and the indicator regions (3.5-6.0 $Å^{-1}$ and 7.5-10.0 $Å^{-1}$, respectively – Marcus et al., 2004). In particular, the splitting of the features at ~7.8 $Å^{-1}$ and ~9.0 $Å^{-1}$ (arrows in Fig. 8a) are indicative of a high Mn(III) content, of the systematic elongation of Mn(III) octahedra along the *a* axis, and of their ordered distribution in rows parallel to the *b* axis (Marcus et al., 2004; Gaillot et al., 2007), typical features for triclinic birnessite (Webb, 2005; Atkins et al., 2014; Yin et al., 2014). With increasing Ni content, the ~7.8 $Å^{-1}$ feature becomes less pronounced even though its position remains unchanged, consistent with the similar Mn(III) contents of all layered precursors (Table 3) and with the similar overall frequency of the EXAFS spectra of these samples (Gaillot et al., 2007). The steady lowering of the ~7.8 $Å^{-1}$ feature resolution is thus most likely related either to disorder in the distribution of elongated Mn(III) octahedral or to some randomness in the direction of the elongation, consistent with the evolution of XRD patterns with increasing Ni content. The split ~9.0 $Å^{-1}$ feature observed for Bir and NiB1 also turns into a broad and more symmetrical feature with increasing Ni content and the induced vanishing of the sharp high-frequency contribution.

In k-space Mn K-edge EXAFS spectra of Tod and NiT1 exhibit sharp features at ~8.0 and ~9.2 $Å^{-1}$ that are typical for todorokite (Webb, 2005; Bodeï et al., 2007; Feng et al., 2010; Atkins et al., 2014). These two features essentially decrease in intensity at higher Ni content. In addition, the ~9.2 $Å^{-1}$ feature shifts to lower wave numbers in

NiT samples compared to Tod and NiB1 (Fig. 8b). EXAFS spectra of Ni-rich NiT samples and their Fourier transforms (FTs) are actually alike those of their corresponding layered precursors (Figs. 9a-b), consistent with the similar structure of the MnO_2 layer in both birnessite and asbolane. On the contrary, spectra obtained for Ni-free Bir and Tod differ significantly, as expected for layered and tunnel manganese oxides (Fig. 9c). In particular, the FTs of these spectra show a clear shortening of the average Mn-Me_E distance in Tod compared to Bir, as shown by the shift of the imaginary part of the FT (Fig. 9d, arrow). In addition, Tod FT shows a clear maximum at $R + \Delta R$ ~ 3.0 Å, typical of Mn-Me_C pairs, which is not observed for its Bir precursor. For both Ni-free and Ni-rich samples, Mn-O distances are similar in both layered precursors and corresponding reflux products, consistent with their similar Mn AOS.

3.9.3. Ni K-edge EXAFS

EXAFS spectra collected at the Ni K-edge are similar for both NiB samples, on the one hand, and NiT, on the other hand (Fig. 10), thus implying similar Ni speciation in each of the two sample groups. Although it was not possible to obtain a decent fit to this data using a linear combination fitting and available Ni reference spectra, similarity of the hydrated Ni(II) spectrum with collected spectra suggests that this species possibly prevails in all samples. In addition, the evolution of Ni speciation during the reflux process was assessed by fitting EXAFS spectra of reflux products as a linear combination of their respective NiB precursors and of Ni reference spectra (Fig. S4). For all NiT samples, a good fit was obtained with ~15% of a $Ni(OH)_2$ contribution in addition to the layered precursor (Table S2), consistent with the polymerization of a partial $Ni(OH)_2$ layer in birnessite interlayers to form an asbolane-like structure.

3.10. Pair distribution functions (G(r))

Atomic PDFs computed from Tod, NiT10, and NiT20 high-energy X-ray

scattering patterns show similar peak positions (Fig. 11), indicative of similar local structures (Zhu et al., 2012) as expected from the major contribution of layers/ribbons of edge-sharing MnO_6 octahedra in both layered precursors and reflux products. Consistently, the maxima at ~1.90 Å, ~2.90 Å, and ~3.50 Å essentially correspond to the first neighbor Mn-O, to edge-sharing Mn-Me, and to a combination of corner-sharing Mn-Me and of second neighbor Mn-O atomic pairs, respectively (Zhu et al., 2012). The increased intensity of the ~3.50 Å maximum and the decreased intensity of the one at ~5.00 Å in the PDF of Tod compared to NiT10 and NiT20 are typical of the prevalence of tunnel structures in the former sample and of layered structures in the latter (Grangeon et al., 2015). The ~5.00 Å maximum is mainly related indeed to second neighbor Mn-Mn pairs (Fig. S4 – Zhu et al., 2012), that are favored by the lateral extension of MnO_2 layers. Finally, the peak at ~4.50 Å is most likely related to Mn2-Mn2 and Mn4-Mn4 pairs across "holes" in tunnel walls, floors, and ceilings (Fig. S6), consistent with the increased intensity of this ~4.50 Å peak with decreasing tunnel size (Zhu et al., 2012).

Differential PDF (d-PDF) can be calculated to assess more precisely the specific modifications affecting the reflux products, and more especially the broadening of the ~1.90 and 2.90 Å peaks towards high d-values with increasing Ni content (Fig. 11). The d-PDF curves obtained for NiT10 and NiT20, both show a first peak at ~2.05 Å typical for Ni-O pairs (Manceau et al., 2007a,b; Peacock and Sherman, 2007a,b; Yin et al., 2012; Kwon et al., 2013; Simanova et al., 2015; Atkins et al., 2016). A second peak, similar in both d-PDF curves, is visible at ~3.05 Å. This second peak is intermediate between those calculated Ni-Ni pairs in NiO and $Ni(OH)_2$, consistent with the presence of both compounds in the reflux products identified from XRD data (Figs. 1, 2).

4. DISCUSSION

4.1. Structural transformation of layered precursors

Addition of Ni during the synthesis of layered precursors does not impact significantly their crystal structure. In particular, the Mn(III) content of layered precursors remains about constant at ~1/3 (Table 3) whatever the initial Ni content. Consistently, XRD results (Fig. 1) show that layer symmetry remains orthogonal ($a > b\sqrt{3}$) for all precursors, indicative of the systematic elongation of distorted Mn(III) octahedra along the *a* axis and of their ordered distribution. FTs of the EXAFS spectra consistently show similar Mn-Me_E distances in all layered precursors (not shown). Both XRD patterns and EXAFS spectra of layered precursors are significantly modified when increasing the Ni content, however. These changes reveal an increased disorder in the orientation of Mn(III) octahedra and/or in their distribution.

The increasing intensity of the ~4.6 Å diffraction maximum with increasing Ni content indicates that part of Ni initially introduced in solution actually precipitates as Ni (hydr)oxide. The presence of Ni in the interlayers of NiB15 and NiB20 is attested by the presence of two planes of interlayer water molecules, consistent with its more negative hydration enthalpy compared to Na^+ (Smith, 1977; Johnson and Post, 2006), in these fresh samples. All Ni species, including the two mentioned above, are readily mobilized by the acid treatment (Fig. 5c), and it is thus reasonable to hypothesize that no Ni(II) cations are incorporated in the octahedral layer. Similarly, the orthogonal layer symmetry is typical of octahedral layers containing few vacant layer sites (Drits et al., 1998; Lanson et al., 2000), if any, and the presence of Ni(II) cations sorbed above or below such vacant sites is thus unlikely.

Although weakly bound to the layered precursors, the presence of Ni(II) significantly impacts their transformation during the reflux process. Bir, a typical triclinic birnessite, converts readily and completely to an ***a***-disorder todorokite (Wu et al., 2019). With increasing Ni content, disorder increases together with the proportion of non-ideal 3×n tunnel sizes forming trilling patterns. In addition, platy crystals are visible in all reflux products, their relative abundance increasing with increasing Ni content with only minimal fragments of tunnel oxides being detected in NiT15 and NiT20 (Fig. 4). Platy crystals are most likely asbolane, as shown by the prevalence of

this phyllomanganate hosting an incomplete octahedral layer of metal (hydr)oxides in their interlayers in Ni-rich reflux products. These incomplete brucite-like octahedral layers are dissolved by the acid treatment, leading to birnessite-like structures (Fig. 5e). As reported in the early work of Chukhrov and coworkers on natural asbolane (Chukhrov, 1982; Chukhrov et al., 1987), XRD diffraction patterns of asbolane are characterized by high $I_{4.8}/I_{9.6}$ intensity ratios. Such high $I_{4.8}/I_{9.6}$ intensity ratios are commonly reported for "todorokite", especially when synthesized in the presence of metallic elements such as Co, Ni, Cu, Zn, Er, La, etc (Shen et al., 1994; Tian et al., 1997; Ching et al., 1999; Luo et al., 1999). In the present study, the combined use of XRD simulation, anomalous XRD, HRTEM, thermogravimetric analysis, and nitric acid treatment allowed uncovering the actual nature of this seldom described phyllomanganate, but its formation may be far more common than previously reported in these experimental studies.

As shown in Fig. 2e, this $I_{4.8}/I_{9.6}$ intensity ratio strongly depends on the completeness of the interlayer brucite-like octahedral layer, and the ratio determined for NiT15 and NiT20 corresponds to a ~50% completeness of the $Ni(OH)_2$ octahedral layer. This interlayer occupancy is much higher than possibly achieved with the sole presence of Ni(II) in these octahedral layers as Ni / (Ni+Mn) ratios are 8-12% in these samples, with part of the Ni present as Ni (hydr)oxide. It is thus likely that Mg cations contribute to the electron density at the interlayer mid-plane, in addition to Ni. As Mg scattering factor is lower than that of Ni, the actual completeness of the interlayer brucite-like layer is likely higher than 50%.

4.2. Differentiation of asbolane and todorokite.

Although the $I_{4.8}/I_{9.6}$ intensity ratio strongly depends on the completeness of the interlayer brucite-like octahedral layer, a 4.8 Å peak stronger than its 9.6 Å counterpart is a possible indication of the presence of the phyllomanganate asbolane, rather than the tectomanganate todorokite, in reaction products, or in natural samples. The two compounds indeed share these two interplanar distances. With its two planes

of interlayer H_2O molecules, buserite also exhibits similar periodicity but a gentle heating (to ~100°C) should lead to the partial dehydration of interlayer cations and to the ~7.2 Å periodicity typical of birnessite (Fig. S1 – Johnson and Post, 2006). Furthermore, buserite is unlikely to have a high enough content of interlayer cations to induce a $I_{4.8}/I_{9.6}$ ratio higher than 1.0.

Although values of this ratio higher than 1.0 are typically observed for asbolane, the partial exchange of Mg present in todorokite tunnels by cations having a higher electronic content (such as Ni and other divalent metal cations) can also lead to such high $I_{4.8}/I_{9.6}$ ratios (Fig. 11), thus not allowing an unambiguous differentiation between asbolane and todorokite. In this search for an unquestionable differentiation between asbolane and todorokite, the nitric acid treatment proposed by Wu et al. (2019) thus appears as a simple and reliable method. In the case of asbolane, dissolution of the interlayer brucite-like layer induced by the treatment leads indeed to a collapse of the layer-to-layer distance to the ~7.2 Å periodicity. On the contrary, periodicities are maintained for todorokite, the tectomanganate framework being unaltered, and positions of XRD maxima are thus unchanged.

4.3. The role of Mn(III) and interlayer species during the transformation

It is now accepted that the presence of a high Mn(III) content (>25-30%) in layered precursors is required for their conversion to tectomanganates. This pivotal role is most likely related to the steric strains induced by the presence of Jahn-Teller distorted Mn(III) octahedra in the octahedral layers. Migration of these Mn(III) cations from layer to interlayer or layer kinking at these structurally weak points contribute to building tunnel walls (Grangeon et al., 2008, 2014; Atkins et al., 2014, 2016; Yang et al., 2018). In the present case, the ordered distribution of Mn(III) cations in rows parallel to the *b* axis and separated from each other along the *a* axis by two rows of Mn(IV) creates a structurally weak point favorable to the formation of tunnels walls (Atkins et al., 2014; Grangeon et al., 2014). Consistently, the initial Ni-free precursor Bir, a triclinic birnessite, was fully converted to todorokite. Similar

transformation of triclinic birnessite to tunnel structures was previously reported in the literature although 3×3 tunnels were not systematically obtained (Yang et al., 2018). Furthermore, the actual distribution and orientation of Mn(III) octahedra present in the MnO_2 layer do not appear to be key factors for the phyllomanganate-to-tectomanganate conversion as tectomanganates were obtained from hexagonal birnessite precursors in which Mn(III) octahedra are distributed and/or oriented at random (Grangeon et al., 2008, 2014; Atkins et al., 2014, 2016; Zhao et al., 2015). The absence of transformation of NiB precursors to tunnel structures thus does not appear to be related to their Mn(III) content, which is similar to or higher than that of the Ni-free Bir.

As layers of all NiB precursors are essentially devoid of Ni, both in the octahedral layer and sorbed above/below vacant layer sites, the absence of transformation of these precursors to tunnel structures is thus likely due to kinetic effects favoring the formation of asbolane. Specifically, polymerization of Ni as $Ni(OH)_2$ fragments in the interlayers of initial birnessite/buserite (Fig. S5, Table S2) is favored over the conversion to tectomanganates. In turn, the presence of interlayer $Ni(OH)_2$ fragments likely impedes the migration of Mn(III) from the layer to the interlayer thus preventing the conversion to tectomanganates. Such competing effects are supported also by the increase of (Mg + Ni)/Mn ratios with increasing Ni content (Table 1) and are likely to occur with a variety of other hydrolysable metal cations. Consistently, "todorokite" containing divalent metal cations and displaying high $I_{4.8}/I_{9.6}$ ratios possibly indicate the presence of asbolane-like structure. Such competing effects might contribute also to the prevalence of phyllomanganates over tectomanganates in natural environments (Wu et al., 2019).

4.4. Negative influence of Ni and Co on the phyllo-to-tectomanganate transformation: Contrasting mechanisms

Both in the present work investigating the possible transformation of Ni-containing layered precursors to tectomanganates and in the related study

investigating a similar process for Co-containing layered precursors, tectomanganate formation was inhibited, totally (Ni) or partially (Co) for Me-rich precursors. The origin of these similar negative impacts differs however for the two metals. In the present case, layered precursors contain sufficient amounts of Mn(III) (~1/3) to trigger the transformation, as Ni(II) is not structurally incorporated in the precursors. As discussed above, polymerization of $Ni(OH)_2$ fragments in birnessite interlayers is kinetically favored over migration of Mn(III) from the layer to the interlayer, or layer kinking, however, leading to the formation of asbolane rather than tectomanganates. In contrast and consistent with previous reports (Manceau et al., 1997; Yu et al., 2012; Kwon et al., 2013; Simanova and Pena, 2015; Yin et al., 2015), Co(II) is readily oxidized by birnessite during the formation of initial layered precursors with Co(III) being structurally incorporated in these precursors owing to the similar ionic radii of Co(III) and Mn(IV) (Wu et al., 2019). The symmetry of layered precursors is increased from orthogonal to hexagonal. As a consequence, the content of Mn(III) in Co-containing layered precursors is lowered and does not allow triggering the transformation to tunnel structures (Grangeon et al., 2008, 2014; Atkins et al., 2014, 2016). In both cases, little Me is released to solution during the reflux process and Me cations are structurally incorporated in the reflux products (~20% and ~80% for Ni and Co, from the nitric acid experiments and EXAFS simulation, respectively) thus enhancing their sequestration in both tecto- and phyllomanganates.

4.5. The fate of Nickel during the transformation of layered precursors

Previous studies have consistently shown that Ni can be incorporated in the birnessite structure, either within the octahedral layer or sorbed at vacant layers sites (Peacock and Sherman, 2007b; Grangeon et al., 2008, 2017; Peacock, 2009; Peña et al., 2010; Yin et al., 2012; Kwon et al., 2013; Yin et al., 2014; Simanova et al., 2015; Atkins et al., 2016; Lefkowitz and Elzinga, 2017), consistent with natural occurrences (Bodeï et al., 2007; Manceau et al., 2007a,b; Peacock and Sherman, 2007a). In their literature review, Grangeon et al. (2017) showed that the fraction of Ni structurally

incorporated in birnessite octahedral layers may be high (up to ~50%) only for low Ni content (~1%), as reported for natural samples (Bodeï et al., 2007; Manceau et al., 2007a,b; Peacock and Sherman, 2007a). Structural incorporation of Ni(II) in the octahedral layer appears to be enhanced by circumneutral pH conditions and time (Manceau et al., 2007b; Peacock and Sherman, 2007b; Peacock, 2009; Peña et al., 2010). Competitive sorption at TCS/DCS sites has been proposed also as a mechanism favoring structural incorporation in the octahedral layer (Lefkowitz and Elzinga, 2017). Some studies report the prevalence of Ni sorbed at TCS/DCS sites even for Ni/Mn ratios higher than 10%, however (Manceau et al., 2007a,b; Peña et al., 2010; Yin et al., 2012; Simanova et al., 2015; Grangeon et al., 2017). In such cases, sorption of Ni(II) as inner sphere complexes is favored by the presence of vacant octahedral sites and is thus negatively correlated with the Mn(III) content. Consistently, in our study structural incorporation of Ni in vacancy-free NiB precursors appears very limited. In NiB layered precursors, Ni is rather present both as Ni (hydr)oxide and as hydrated cations in birnessite/buserite interlayers, as shown by the increased hydration of Ni-rich precursors (Figs. 1, S1). The influence of Ni on phyllomanganate hydration has been reported also for natural samples in which buserite (or 10 Å vernadite) abundance increases with increasing Ni content (Bodeï et al., 2007; Manceau et al., 2007a).

As discussed above, hydrated Ni(II) initially present in birnessite interlayers are readily stabilized during the reflux products by forming $Ni(OH)_2$ fragments (Fig. S5, Table S2), consistent with previous experiments with vacancy-free phyllomanganate precursors (Feng et al., 2001). Polymerization of $Ni(OH)_2$ brucite-like octahedral layers in phyllomanganate interlayers is consistent also with the natural predominance of asbolane in Ni-rich environments (NiO ~10-20 wt.%, – Chukhrov, 1982; Chukhrov et al., 1987; Roque-Rosell et al., 2010; Ploquin et al., 2018) . Although the Mn AOS of his synthetic samples (~4.0) was favorable for Ni sorption at layer vacancy sites, Manceau et al. (2007b) also reported the overwhelming presence of Ni as $Ni(OH)_2$ at high Ni content (Ni/Mn ratio of ~0.10 and ~0.18 at pH 4 and 7, respectively), despite experimental conditions supposed to prevent $Ni(OH)_2$ precipitation. The reflux

process appears to have little influence on the Ni (hydr)oxide formed together with the layered precursors, as evidenced by the stability of the corresponding maximum at ~4.6 Å in the reflux products (Fig. 1b). Finally, part of Ni (~20 %) is stabilized during the reflux process, as shown by the incomplete Ni release during acid treatment (Fig. 5d). Stabilized Ni is possibly structurally incorporated in the reflux products. On the contrary, Atkins et al. (2016) reported no structural incorporation of Ni(II) during the formation of todorokite from a Ni-bearing birnessite precursor (~1 wt% Ni in hexagonal birnessite). They reported also a decrease in the Ni content of their reflux products, whereas in our experimental conditions stability of Ni/(Mn+Ni) ratios (Table 1) indicates that all Ni initially present in layered precursors is retained during the reflux process.

5. CONCLUSION

The present study reports on the association of weakly bound Ni species (hydrated Ni, Ni (hydr)oxides) with phyllomanganates, that possibly prevail in natural Ni-rich (>10% NiO) manganates. Whatever their Ni content, prepared phyllomanganates systematically exhibit an orthogonal layer symmetry, indicative of a high Mn(III) content and of a minimal number of octahedral layer vacancies. Ni is essentially present as charge-compensating hydrated Ni(II) and as Ni (hydr)oxide, with no detectable Ni(II) sorbed or structurally incorporated in the phyllomanganate structure.

Despite their high content of Mn(III), a favorable condition for their conversion to tectomanganates, absolane rather than tectomanganates forms during the reflux processing of these Ni-rich phyllomanganates. Asbolane formation results from the kinetically favored polymerization of fragments of $Ni(OH)_2$ octahedral layers in birnessite interlayers. The structure of the initial manganate layers is essentially unaffected by this transformation.

Formation of asbolane, rather than todorokite, may actually be more frequent than

reported in the literature owing to the similar periodicities in both compounds. High values (> 1) of the $I_{4.8}/I_{9.6}$ intensity ratio may suggest the presence of this seldom described phyllomanganate. Acid nitric treatment, aiming at the dissolution of the island-like interlayer $Ni(OH)_2$ layer, represents an easy and unambiguous way to differentiate asbolane from todorokite which is unaffected by the treatment.

Both the presence of Co and Ni in synthesized phyllomanganates impede their transformation to tectomanganates when refluxed, the origin of this similar impact being different for the two metals, however. Oxidation of Co(II) sorbed on the MnO_2 layer and the subsequent structural incorporation of Co(III) in the octahedral layer releases the steric strains related to the presence of Jahn-Teller distorted Mn(III) octahedra, which is required for the phyllomanganate-to-tectomanganate conversion. In contrast, the presence of hydrated Ni(II) favors the polymerization of fragments of $Ni(OH)_2$ octahedral layers, that in turn prevents the formation of tectomanganates despite the favorable presence of Mn(III) in the octahedral MnO_2 layer. In both cases, "foreign" metal cations are retained in the refluxed products, with contrasting ratios of structural incorporation.

ACKNOWLEDGMENTS

Caroline Peacock (Leeds University, UK) is thanked for providing Ni K-edge EXAFS data of Bir-Ni_S and Bir-Ni_V references. The authors are grateful to Mengqiang Zhu (University of Wyoming, Laramie, Wy, USA) for helping collect high-energy X-ray scattering data and providing Ni(II)-H_2O EXAFS reference. This work is supported by the National Key Research and Development Program of China (No. 2016YFD0800400) and the Natural Science Foundations of China (No. 41571448). Xionghan Feng, Bruno Lanson, and Zhongkuan Wu are supported by a Cai Yuanpei program between the Key Laboratory of Arable Land Conservation (Wuhan, China) and ISTerre (Grenoble, France)

REFERENCES

Atkins A.L., Shaw S. and Peacock C.L. (2014) Nucleation and growth of todorokite from birnessite: Implications for trace-metal cycling in marine sediments. *Geochim. Cosmochim. Acta* 144, 109-125.

Atkins A.L., Shaw S. and Peacock C.L. (2016) Release of Ni from birnessite during transformation of birnessite to todorokite: Implications for Ni cycling in marine sediments. *Geochim. Cosmochim. Acta* **189**, 158-183.

Bish D.L. and Post J.E. (1989) Thermal behavior of complex, tunnel-structure manganese oxides. *Amer. Mineral.* **74**, 177-186.

Bodeï S., Manceau A., Geoffroy N., Baronnet A. and Buatier M. (2007) Formation of todorokite from vernadite in Ni-rich hemipelagic sediments. *Geochim. Cosmochim. Acta* **71**, 5698-5716.

Burlet C. and Vanbrabant Y. (2015) Study of the spectro-chemical signatures of cobalt-manganese layered oxides (asbolane-lithiophorite and their intermediates) by Raman spectroscopy. *J. Raman Spectr.* **46**, 941-952.

Burns R.G., Burns V.M. and Stockman H.W. (1983) A review of the todorokite-buserite problem; implications to the mineralogy of marine manganese nodules. *Amer. Mineral.* **68**, 972-980.

Ching S., Krukowska K.S. and Suib S.L. (1999) A new synthetic route to todorokite-type manganese oxides. *Inorg. Chim. Acta* **294**, 123-132.

Chukhrov F.V. (1982) Crystallochemical nature of Co-Ni asbolan. *Int. Geol. Rev.* **24**, 598-604.

Chukhrov F.V., Drits V.A. and Gorshkov A.I. (1987) Structural Transformations of Manganese Oxides in Oceanic Nodules. *Int. Geol. Rev.* **29**, 110-121.

Cui H.J., Liu X.W., Tan W.F., Feng X.H., Liu F. and Ruan H.D. (2008) Influence of Mn(III) availability on the phase transformation from layered buserite to tunnel-structured todorokite. *Clay Clay Miner.* **56**, 397-403.

Drits V.A., Lanson B., Gorshkov A.I. and Manceau A. (1998) Substructure and superstructure of four-layer Ca-exchanged birnessite. *Amer. Mineral.* **83**, 97-118.

Drits V.A., Silvester E., Gorshkov A.I. and Manceau A. (1997) Structure of synthetic monoclinic Na-rich birnessite and hexagonal birnessite: I. Results from X-ray diffraction and selected-area electron diffraction. *Amer. Mineral.* **82**, 946-961.

Duff M.C., Hunter D.B., Triay I.R., Bertsch P.M., Reed D.T., Sutton S.R., Shea-McCarthy G., Kitten J., Eng P. and Chipera S.J. (1999) Mineral associations and average oxidation states of sorbed Pu on tuff. *Environ. Sci. Technol.* **33**, 2163-2169.

Fan R. and Gerson A.R. (2015) Synchrotron micro-spectroscopic examination of Indonesian nickel laterites. *Amer. Mineral.* **100**, 926-934.

Feitknecht W., Christen H.R. and Studer H., Z. (1956) Zur Kenntnis der höhern Nickelhydroxyde; die Oxydation von Nickelhydroxyd. *Z. Anorg. Chem.* **283**, 88-95 (in German).

Feng Q., Xu Y., Kajiyoshi K. and Yanagisawa K. (2001) Hydrothermal Soft Chemical Synthesis of $Ni(OH)_2$–Birnessite Sandwich Layered Compound and Layered $LiNi_{1/3}Mn_{2/3}O_2$. *Chem. Lett.* **30**, 1036-1037.

Feng X.H., Tan W.F., Liu F., Wang J.B. and Ruan H.D. (2004) Synthesis of todorokite at atmospheric pressure. *Chem. Mater.* **16**, 4330-4336.

Feng X.H., Zhu M., Ginder-Vogel M., Ni C., Parikh S.J. and Sparks D.L. (2010) Formation of nano-crystalline todorokite from biogenic Mn oxides. *Geochim. Cosmochim. Acta* **74**, 3232-3245.

Fuertes A., Da Costa-Serra J.F. and Chica A. (2012) New Catalysts based on Ni-Birnessite and Ni-Todorokite for the Efficient Production of Hydrogen by Bioethanol Steam Reforming. *Energ. Proc.* **29**, 181-191.

Gaillot A.-C., Drits V.A., Manceau A. and Lanson B. (2007) Structure of the synthetic K-rich phyllomanganate birnessite obtained by high-temperature decomposition of $KMnO_4$. *Micropor. Mesopor. Mater.* **98**, 267-282.

Gaillot A.-C., Flot D., Drits V.A., Manceau A., Burghammer M. and Lanson B. (2003) Structure of synthetic K-rich birnessite obtained by high-temperature decomposition of $KMnO_4$. I. Two-layer polytype from 800 C experiment. *Chem. Mater.* **15**, 4666-4678.

Golden D.C., Chen C.C. and Dixon J.B. (1986) Synthesis of todorokite. *Science* **231**, 717-719.

Golden D.C., Chen C.C. and Dixon J.B. (1987) Transformation of birnessite to buserite, todorokite, and manganite under mild hydrothermal treatment. *Clay Clay Miner.* **35**, 271-280.

Grangeon S., Fernandez-Martinez A., Claret F., Marty N., Tournassat C., Warmont F. and Gloter A. (2017) In-situ determination of the kinetics and mechanisms of nickel adsorption by nanocrystalline vernadite. *Chem. Geol.* **459**, 24-31.

Grangeon S., Fernandez-Martinez A., Warmont F., Gloter A., Marty N., Poulain A. and Lanson B. (2015) Cryptomelane formation from nanocrystalline vernadite precursor: a high energy X-ray scattering and transmission electron microscopy perspective on reaction mechanisms. *Geochem. Trans.* **16**, 12.

Grangeon S., Lanson B. and Lanson M. (2014) Solid-state transformation of nanocrystalline phyllomanganate into tectomanganate: influence of initial layer and interlayer structure. *Acta Crysrtallogr. B* **70**, 828-838.

Grangeon S., Lanson B., Lanson M. and Manceau A. (2008) Crystal structure of Ni-sorbed synthetic vernadite: a powder X-ray diffraction study. *Mineral. Mag.* **72**, 1279-1291.

Hall D.S., Lockwood D.J., Bock C. and MacDougall B.R. (2015) Nickel hydroxides and related materials: a review of their structures, synthesis and properties. *Proc. R. Soc. A* **471**, 20140792.

Johnson E.A. and Post J.E. (2006) Water in the interlayer region of birnessite: Importance in cation exchange and structural stability. *Amer. Mineral.* **91**, 609-618.

Julien C.M., Massot M. and Poinsignon C. (2004) Lattice vibrations of manganese oxides. *Spectroc. Acta Pt. A-Molec. Biomolec. Spectr.* **60**, 689-700.

Kasten S., Glasby G.P., Schulz H.D., Friedrich G. and Andreev S.I. (1998) Rare earth elements in manganese nodules from the South Atlantic Ocean as indicators of oceanic bottom water flow. *Mar. Geol.* **146**, 33-52.

Kwon K.D., Refson K. and Sposito G. (2013) Understanding the trends in transition metal sorption by vacancy sites in birnessite. *Geochim. Cosmochim. Acta* **101**, 222-232.

Lanson B., Drits V.A., Feng Q. and Manceau A. (2002b) Structure of synthetic Na-birnessite: Evidence for a triclinic one-layer unit cell. *Amer. Mineral.* **87**, 1662-1671.

Lanson B., Drits V.A., Gaillot A.-C., Silvester E., Plançon A. and Manceau A. (2002a) Structure of heavy-metal sorbed birnessite: Part 1. Results from X-ray diffraction. Amer. Mineral. 87, 1631-1645.

Lanson B., Drits V.A., Silvester E. and Manceau A. (2000) Structure of H-exchanged hexagonal birnessite and its mechanism of formation from Na-rich monoclinic buserite at low pH. *Amer.*

Mineral. **85**, 826-838.

Lanson B., Marcus M.A., Fakra S., Panfili F., Geoffroy N. and Manceau A. (2008) Formation of Zn–Ca phyllomanganate nanoparticles in grass roots. *Geochim. Cosmochim. Acta* **72**, 2478-2490.

Lefkowitz J.P. and Elzinga E.J. (2017) Structural alteration of hexagonal birnessite by aqueous Mn(II): Impacts on Ni(II) sorption. *Chem. Geol.* **466**, 524-532.

Li W., Harrington R., Tang Y., Kubicki J.D., Aryanpour M., Reeder R.J., Parise J.B. and Phillips B.L. (2011) Differential pair distribution function study of the structure of arsenate adsorbed on nanocrystalline γ-alumina. *Environ. Sci. Technol.* **45**, 9687-9692.

Li Y.F., Zhu S.C. and Liu Z.P. (2016) Reaction Network of Layer-to-Tunnel Transition of MnO_2. *J. Am. Chem. Soc.* **138**, 5371-5379.

Llorca S. (1988) Nouvelles données sur la composition et la structure des asbolanes (Nouvelle-Calédonie). *C. R. Acad. Sci Paris - Série II* **307**, 155-161.

Luo J., Zhang Q., Huang A., Giraldo O. and Suib S.L. (1999) Double-aging method for preparation of stabilized Na− buserite and transformations to todorokites incorporated with various metals. *Inorg. Chem.* **38**, 6106-6113.

Manceau A., Gorshkov A.I. and Drits V.A. (1992a) Structural chemistry of Mn, Co, and Ni in manganese hydrous oxides. I. Information from EXAFS spectroscopy and electron and X-ray diffraction. *Amer. Mineral.* **77**, 1144-1157.

Manceau A., Gorshkov A.I. and Drits V.A. (1992b) Structural chemistry of Mn, Co, and Ni in manganese hydrous oxides. I. Information from XANES spectroscopy. *Amer. Mineral.* **77**, 1133-1143.

Manceau A., Kersten M., Marcus M.A., Geoffroy N. and Granina L. (2007a) Ba and Ni speciation in a nodule of binary Mn oxide phase composition from Lake Baikal. *Geochim. Cosmochim. Acta* **71**, 1967-1981.

Manceau A., Lanson M. and Geoffroy N. (2007b) Natural speciation of Ni, Zn, Ba, and As in ferromanganese coatings on quartz using X-ray fluorescence, absorption, and diffraction. *Geochim. Cosmochim. Acta* **71**, 95-128.

Manceau A., Lanson M. and Takahashi Y. (2014) Mineralogy and crystal chemistry of Mn, Fe, Co, Ni, and Cu in a deep-sea Pacific polymetallic nodule. *Amer. Mineral.* **99**, 2068-2083.

Manceau A., Llorca S. and Calas G. (1987) Crystal chemistry of cobalt and nickel in lithiophorite and asbolane from New Caledonia. *Geochim. Cosmochim. Acta* **51**, 105-113.

Manceau A., Marcus M.A. and Grangeon S. (2012) Determination of Mn valence states in mixed-valent manganates by XANES spectroscopy. *Amer. Mineral.* **97**, 816-827.

Manceau A., Silvester E., Bartoli C., Lanson B. and Drits V.A. (1997) Structural mechanism of Co^{2+} oxidation by the phyllomanganate buserite. *Amer. Mineral.* **82**, 1150-1175.

Manceau A., Tamura N., Marcus M.A., MacDowell A.A., Celestre R.S., Sublett R.E., Sposito G. and Padmore H.A. (2002) Deciphering Ni sequestration in soil ferromanganese nodules by combining X-ray fluorescence, absorption, and diffraction at micrometer scales of resolution. *Amer. Mineral.* **87**, 1494-1499.

Marcus M.A., Manceau A. and Kersten M. (2004) Mn, Fe, Zn and As speciation in a fast-growing ferromanganese marine nodule. *Geochim. Cosmochim. Acta* **68**, 3125-3136.

Nicolas-Tolentino E., Tian Z.-R., Zhou H., Xia G. and Suib S.L. (1999) Effects of Cu^{2+} ions on the structure and reactivity of todorokite-and cryptomelane-type manganese oxide octahedral molecular sieves. *Chem. Mater.* **11**, 1733-1741.

Ohnuki T., Jiang M., Sakamoto F., Kozai N., Yamasaki S., Yu Q., Tanaka K., Utsunomiya S., Xia X., Yang K. and He J. (2015) Sorption of trivalent cerium by a mixture of microbial cells and manganese oxides: Effect of microbial cells on the oxidation of trivalent cerium. *Geochim. Cosmochim. Acta* **163**, 1-13.

Ohta A. and Kawabe I. (2001) REE(III) adsorption onto Mn dioxide (delta-MnO_2) and Fe oxyhydroxide: Ce(III) oxidation by delta-MnO_2. *Geochim. Cosmochim. Acta* **65**, 695-703.

Onda A., Hara S., Kajiyoshi K. and Yanagisawa K. (2007) Synthesis of manganese oxide octahedral molecular sieves containing cobalt, nickel, or magnesium, and the catalytic properties for hydration of acrylonitrile. *Appl. Catal. A. Gen.* **321**, 71-78.

Peacock C.L. (2009) Physiochemical controls on the crystal-chemistry of Ni in birnessite: Genetic implications for ferromanganese precipitates. *Geochim. Cosmochim. Acta* **73**, 3568-3578.

Peacock C.L. and Sherman D.M. (2007a) Crystal-chemistry of Ni in marine ferromanganese crusts and nodules. *Amer. Mineral.* **92**, 1087-1092.

Peacock C.L. and Sherman D.M. (2007b) Sorption of Ni by birnessite: Equilibrium controls on Ni in seawater. *Chem. Geol.* **238**, 94-106.

Peña J., Kwon K.D., Refson K., Bargar J.R. and Sposito G. (2010) Mechanisms of nickel sorption by a bacteriogenic birnessite. *Geochim. Cosmochim. Acta* **74**, 3076-3089.

Ploquin F., Fritsch E., Guigner J.M., Esteve I., Delbes L., Dublet G. and Juillot F. (2018) Phyllomanganate vein-infillings in faulted and Al-poor regoliths of the New Caledonian ophiolite: periodic and sequential crystallization of Ni–asbolane, Alk–birnessite and H–birnessite. *Eur. J. Mineral.*

Post J.E. (1999) Manganese oxide minerals: Crystal structures and economic and environmental significance. *Proc. Nat. Acad. Sci.* **96**, 3447-3454

Post J.E. and Bish D.L. (1988) Rietveld refinement of the todorokite structure. *Amer. Mineral.* **73**, 861-869.

Post J.E., Heaney P.J. and Hanson J. (2003) Synchrotron X-ray diffraction study of the structure and dehydration behavior of todorokite. *Amer. Mineral.* **88**, 142-150.

Qin Z., Yin H., Wang X., Zhang Q., Lan S., Koopal L.K., Zheng L., Feng X. and Liu F. (2018) The preferential retention of ^{VI}Zn over ^{IV}Zn on birnessite during dissolution/desorption. *Appl. Clay Sci.* **161**, 169-175.

Ravel B. and Newville M. (2005) ATHENA and ARTEMIS: interactive graphical data analysis using IFEFFIT. *Phys. Scripta* **2005**, 1007.

Remucal C.K. and Ginder-Vogel M. (2014) A critical review of the reactivity of manganese oxides with organic contaminants. *Envir. Sci.-Proc. Imp.* **16**, 1247-1266.

Roque-Rosell J., Mosselmans J.F.W., Proenza J.A., Labrador M., Gali S., Atkinson K.D. and Quinn P.D. (2010) Sorption of Ni by "lithiophorite-asbolane" intermediates in Moa Bay lateritic deposits, eastern Cuba. *Chem. Geol.* **275**, 9-18.

Shen X., Morey A.M., Liu J., Ding Y., Cai J., Durand J., Wang Q., Wen W., Hines W.A., Hanson J.C., Bai J., Frenkel A.I., Reiff W., Aindow M. and Suib S.L. (2011) Characterization of the Fe-Doped Mixed-Valent Tunnel Structure Manganese Oxide KOMS-2. *J. Phys. Chem. C* **115**, 21610-21619.

Shen Y.-F., Suib S.L. and O'Young C.-L. (1994) Effects of inorganic cation templates on octahedral molecular sieves of manganese oxide. *J. Am. Chem. Soc.* **116**, 11020-11029.

Shen Y.F., Zerger R.P., DeGuzman R.N., Suib S.L., McCurdy L., Potter D.I. and O'Young C.L. (1993) Manganese oxide octahedral molecular sieves: preparation, characterization, and applications.

971 *Science* **260**, 511-515.
972 Sherman D.M. and Peacock C.L. (2010) Surface complexation of Cu on birnessite (δ-MnO2): Controls
973 on Cu in the deep ocean. *Geochim. Cosmochim. Acta* **74**, 6721-6730.
974 Siegel M.D. and Turner S. (1983) Crystalline todorokite associated with biogenic debris in manganese
975 nodules. *Science* **219**, 172-174.
976 Simanova A.A., Kwon K.D., Bone S.E., Bargar J.R., Refson K., Sposito G. and Peña J. (2015) Probing
977 the sorption reactivity of the edge surfaces in birnessite nanoparticles using nickel(II). *Geochim.*
978 *Cosmochim. Acta* **164**, 191-204.
979 Simanova A.A. and Pena J. (2015) Time-Resolved Investigation of Cobalt Oxidation by Mn(III)-Rich
980 delta-MnO_2 Using Quick X-ray Absorption Spectroscopy. *Environ. Sci. Technol.* **49**, 10867-10876.
981 Smith D.W. (1977) Ionic hydration enthalpies. *J. Chem. Educ.* **54**, 540.
982 Song C., Li R., Liu F., Feng X., Tan W. and Qiu G. (2010) Cobalt-doped todorokites prepared by
983 refluxing at atmospheric pressure as cathode materials for Li batteries. *Electrochim. Acta* **55**,
984 9157-9165.
985 Spinks S.C., Uvarova Y., Thorne R., Anand R., Reid N., White A., Ley-Cooper Y., Bardwell N., Gray
986 D., Meadows H. and LeGras M. (2017) Detection of zinc deposits using terrestrial ferromanganese
987 crusts. *Ore Geol. Rev.* **80**, 484-503.
988 Tian Z.-R., Yin Y.-G., Suib S.L. and O'Young C.L. (1997) Effect of Mg^{2+} ions on the formation of
989 todorokite type manganese oxide octahedral molecular sieves. *Chem. Mater.* **9**, 1126-1133.
990 Toner B., Manceau A., Webb S.M. and Sposito G. (2006) Zinc sorption to biogenic
991 hexagonal-birnessite particles within a hydrated bacterial biofilm. *Geochim. Cosmochim. Acta* **70**,
992 27-43.
993 Turner S. and Buseck P.R. (1981) Todorokites: A new family of naturally occurring manganese oxides.
994 *Science* **212**, 1024-1027.
995 Wang X., Li W., Harrington R., Liu F., Parise J.B., Feng X. and Sparks D.L. (2013) Effect of
996 ferrihydrite crystallite size on phosphate adsorption reactivity. *Environ. Sci. Technol.* **47**,
997 10322-10331.
998 Wang Z., Lv K., Wang G., Deng K. and Tang D. (2010) Study on the shape control and photocatalytic
999 activity of high-energy anatase titania. *Appl. Catal. B. Envir.* **100**, 378-385.
1000 Webb S.M. (2005) Structural characterization of biogenic Mn oxides produced in seawater by the
1001 marine bacillus sp. strain SG-1. *Amer. Mineral.* **90**, 1342-1357.
1002 Wegorzewski A.V., Kuhn T., Dohrmann R., Wirth R. and Grangeon S. (2015) Mineralogical
1003 characterization of individual growth structures of Mn-nodules with different Ni+Cu content from
1004 the central Pacific Ocean. *Amer. Mineral.* **100**, 2497-2508.
1005 Wu Z., Peacock C.L., Lanson B., Yin H., Zheng L., Chen Z., Tan W., Qiu G., Liu F. and Feng X. (2019)
1006 Transformation of Co-containing birnessite to todorokite: Effect of Co on the transformation and
1007 implications for Co mobility. *Geochim. Cosmochim. Acta* **246**, 21-40.
1008 Xu H., Chen T. and Konishi H. (2010) HRTEM investigation of trilling todorokite and nano-phase
1009 Mn-oxides in manganese dendrites. *Amer. Mineral.* **95**, 556-562.
1010 Yang P., Lee S., Post J.E., Xu H.F., Wang Q., Xu W.Q. and Zhu M.Q. (2018) Trivalent manganese on
1011 vacancies triggers rapid transformation of layered to tunneled manganese oxides (TMOs):
1012 Implications for occurrence of TMOs in low-temperature environment. *Geochim. Cosmochim. Acta*
1013 **240**, 173-190.
1014 Yin H., Feng X., Qiu G., Tan W. and Liu F. (2011a) Characterization of Co-doped birnessites and

application for removal of lead and arsenite. *J. Hazard. Mater.* **188**, 341-349.

Yin H., Li H., Wang Y., Ginder-Vogel M., Qiu G., Feng X., Zheng L. and Liu F. (2014) Effects of Co and Ni co-doping on the structure and reactivity of hexagonal birnessite. *Chem. Geol.* **381**, 10-20.

Yin H., Liu F., Feng X., Liu M., Tan W. and Qiu G. (2011b) Co^{2+}-exchange mechanism of birnessite and its application for the removal of Pb^{2+} and As(III). *J. Hazard. Mater.* **196**, 318-326.

Yin H., Liu Y., Koopal L.K., Feng X., Chu S., Zhu M. and Liu F. (2015) High Co-doping promotes the transition of birnessite layer symmetry from orthogonal to hexagonal. *Chem. Geol.* **410**, 12-20.

Yin H., Tan W., Zheng L., Cui H., Qiu G., Liu F. and Feng X. (2012) Characterization of Ni-rich hexagonal birnessite and its geochemical effects on aqueous Pb^{2+}/Zn^{2+} and As(III). *Geochim. Cosmochim. Acta* **93**, 47-62.

Yu Q., Sasaki K., Tanaka K., Ohnuki T. and Hirajima T. (2012) Structural factors of biogenic birnessite produced by fungus Paraconiothyrium sp. WL-2 strain affecting sorption of Co2+. *Chem. Geol.* **310-311**, 106-113.

Yu Q.Q., Sasaki K., Tanaka K., Ohnuki T. and Hirajima T. (2013) Zinc Sorption During Bio-oxidation and Precipitation of Manganese Modifies the Layer Stacking of Biogenic Birnessite. *Geomicrobiol. J.* **30**, 829-839.

Zawadzki D., Maciag L., Kotlinski R.A., Kozub-Budzyn G.A., Piestrzynski A. and Wrobel R. (2018) Geochemistry of cobalt-rich ferromanganese crusts from the Perth Abyssal Plain (E Indian Ocean). *Ore Geol. Rev.* **101**, 520-531.

Zhao H.Y., Liang X.R., Yin H., Liu F., Tan W.F., Qiu G.H. and Feng X.H. (2015) Formation of todorokite from "c-disordered" H^{+}-birnessites: the roles of average manganese oxidation state and interlayer cations. *Geochem. Trans.* **16**, 11.

Zhu M., Farrow C.L., Post J.E., Livi K.J.T., Billinge S.J.L., Ginder-Vogel M. and Sparks D.L. (2012) Structural study of biotic and abiotic poorly-crystalline manganese oxides using atomic pair distribution function analysis. *Geochim. Cosmochim. Acta* **81**, 39-55.

Table 1

Chemical composition and specific surface area of layered precursors and reflux products

Samples	Mn wt. %	Ni wt. %	Ni/(Mn+Ni) mol%	Mg wt. %	(Mg+Ni)/Mn mol%	SSA (m^2/g)
Bir	55.4(1.0)	--	--	--	--	--
NiB1	54.1(1.1)	0.39(1)	0.67	--	--	--
NiB5	53.7(1.0)	1.86(4)	3.18	--	--	--
NiB10	51.2(1.0)	3.89(7)	5.98	--	--	--
NiB15	47.3(1.7)	5.32(3)	8.71	--	--	--
NiB20	44.8(1.8)	7.14(7)	11.50	--	--	--
Tod	54.4(2.1)	--	--	3.95(8)	16.4	90.7
NiT1	54.3(8)	0.33(1)	0.57	3.51(12)	16.2	--
NiT5	54.2(6)	1.57(2)	2.57	3.12(2)	15.6	93.7
NiT10	52.7(6)	3.79(1)	5.94	2.61(2)	17.5	119.7
NiT15	52.4(1.2)	5.66(9)	8.41	2.59(6)	20.4	109.0
NiT20	49.2(9)	7.74(2)	11.38	2.11(2)	22.5	106.8

Table 2.

Weight loss of layered precursors and reflux products over specific temperature intervals

Temperature (°C)	Weight loss/%				
	Bir	NiB5	NiB10	NiB15	NiB20
RT-100	2.45	2.87	2.64	2.84	9.25
100-170	8.43	7.14	6.54	5.73	4.87
170-400	1.78	4.10	4.74	5.78	6.72
Total	17.38	19.20	18.85	19.15	25.31
	Tod	NiT5	NiT10	NiT15	NiT20
RT-110	2.75	2.93	3.39	3.90	4.12
110-240	8.05	7.68	7.43	6.57	6.12
240-380	5.47	5.32	5.04	5.34	5.97
380-500	2.69	2.33	2.08	1.93	1.79
500-650	4.50	4.35	4.06	3.75	3.61
Total	23.47	22.61	22.01	21.48	21.60

Table 3.

Fractional and average valence states of Mn obtained for layered precursors and reflux products from the Combo fit of XANES spectra and 1st derivatives. The estimated error for Combo method is ±4% (Manceau et al., 2012; Yin et al., 2015)

Sample	Mn^{2+} at. %	Mn^{3+} at. %	Mn^{4+} at. %	Mn-AOS
Bir	3	26	72	3.69
NiB1	2	25	74	3.71
NiB5	2	30	67	3.64
NiB10	2	31	68	3.66
NiB15	0	31	69	3.69
NiB20	0	35	65	3.65
Tod	2	25	74	3.72
NiT1	1	35	65	3.64
NiT5	3	32	66	3.63
NiT10	2	35	64	3.62
NiT15	1	34	65	3.64
NiT20	0	33	67	3.67

Figure Captions

Fig. 1. XRD patterns of layered precursors (top) and reflux products (bottom). Colors correspond to the Ni/(Ni+Mn) ratio of the samples. Green ticks at the bottom of upper and lower figures indicate the reflections of triclinic birnessite (ICDD #43-1456) and todorokite (ICDD #38-0475), respectively.

Fig. 2. XRD patterns collected for NiT20, NiT15, and Tod at (a) Mn K-edge (6.5 keV), (b) Ni K-edge (8.3 eV), (c) 12.0 keV, and (d) 18.0 keV. Intensities were systematically normalized to the most intense reflection. Colors as in Fig. 1. (e) XRD patterns calculated for an asbolane containing 0.525 $Ni(OH)_2$ in MnO_2 interlayers. Contents of Ni and Mn atoms are reduced by 20% at their respective absorption edges to simulate the anomalous effect.

Fig. 3. FTIR spectra of layered precursors and reflux products (top and bottom, respectively). Colors as in Fig. 1.

Fig. 4. HRTEM images of (a-b): Tod, (c-e): NiT1, (f-h): NiT5, (i-m): NiT1. Numbers in (b) and (d) indicate the number of MnO_6 octahedra defining tunnel width. Arrows in (i) and (l) indicate the direction of fringes bending.

Fig. 5. Proportion of metal cations released during the nitric acid treatment: (a-b): Mn, (c-d): Ni, and (f): Mg. The amount of metal released is normalized to the sample overall metal content (see text for details). (e): XRD patterns of samples treated with nitric acid. Colors as in Fig. 1 except for Bir in (e).

Fig. 6. Thermogravimetric analysis traces obtained for (a) layered precursors and (b) reflux products, and their 1st derivatives (c and d, respectively). 1st derivative curves were smoothed using a Savitzky-Golay filter and a 15 point window. Colors as in Fig. 1.

Fig. 7. XPS O1s spectra obtained for layered precursors and reflux products (left and right, respectively). The thick solid curve represents the best fit to the data (open red squares). Peaks corresponding to O^{2-}, OH^-, and H_2O species are shown in the order of increasing binding energy as dashed purple, dotted-dashed green, and dotted blue lines, respectively. The green dotted line is the difference curve.

Fig. 8. Mn K-edge EXAFS spectra obtained for (a) layered precursors and (b) reflux products. Colors as in Fig. 1.

Fig. 9. Comparison of (a, c) Mn K-edge EXAFS and (b, d) of their FTs (showing both real and imaginary parts) obtained for Ni-rich (Top: NiB15 and NiT15) and Ni-free (bottom: Bir and Tod) layered precursors and corresponding reflux products.

Fig. 10. Comparison of Ni K-edge EXAFS spectra obtained for layered precursors and reflux products with reference spectra. Sample colors as in Fig. 1.

Fig. 11. Pair distribution functions obtained for Ni-rich (NiT10 and NiT20) and Ni-free (Tod) reflux products (top). Middle: d-PDFs relative to Tod PDF data; bottom: PDFs calculated for Ni (hydr)oxides (ICSD #76670 and #28101 for NiO and $Ni(OH)_2$, respectively). Intensities of experimental PDFs and of difference PDFs were normalized to the 2.9-3.1 Å peak.

1107 Fig. 12. Intensity distributions calculated for ideal todorokite (ICDD #38-0475) with
1108 (a) only Mg in todorokite tunnels and (b) with Mg and Ni present in a 1:1 ratio in
1109 todorokite tunnels. In both cases, the model of Post et al. (2003) was modified
1110 assuming the complete filling of the O8 site by H_2O molecules (no cations) and the
1111 presence of 1.0 cation (Mg or Mg+Ni) in the Mg site.

Figure

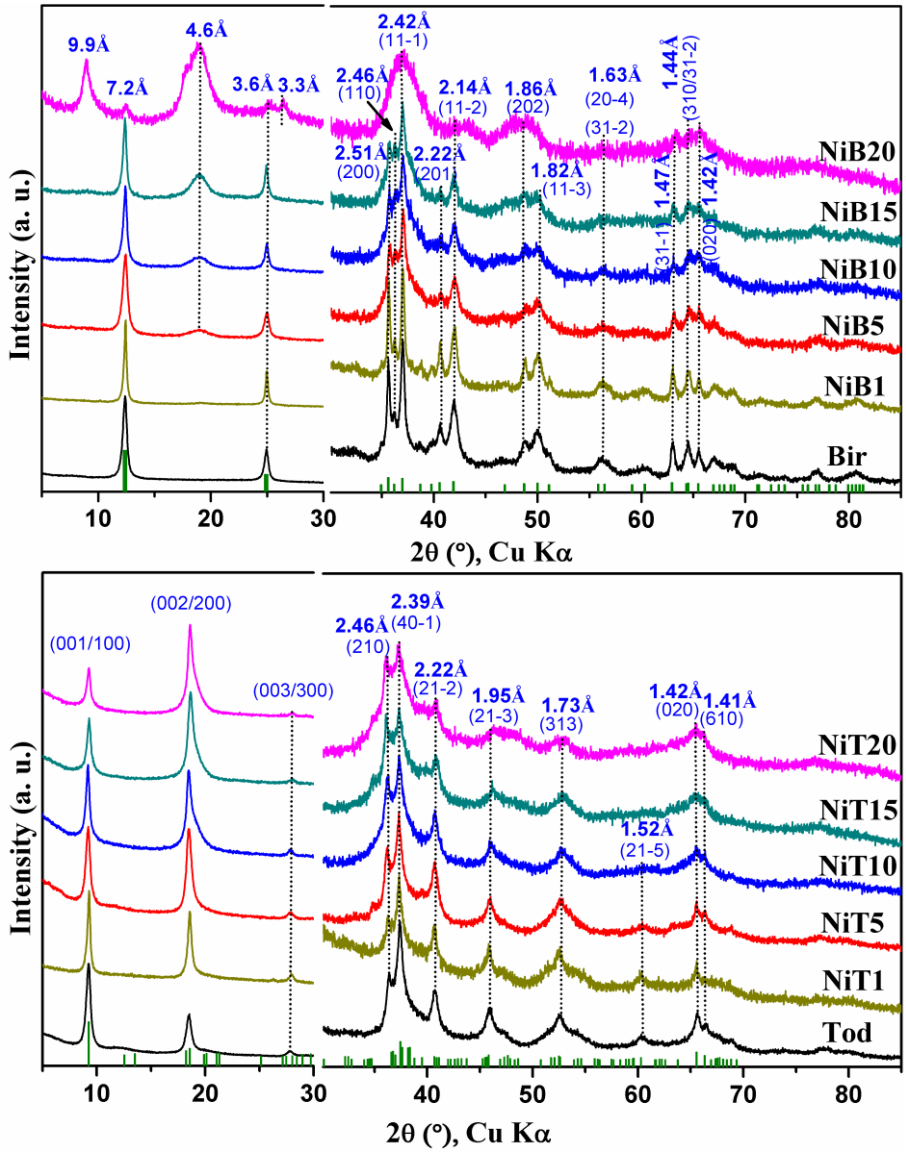
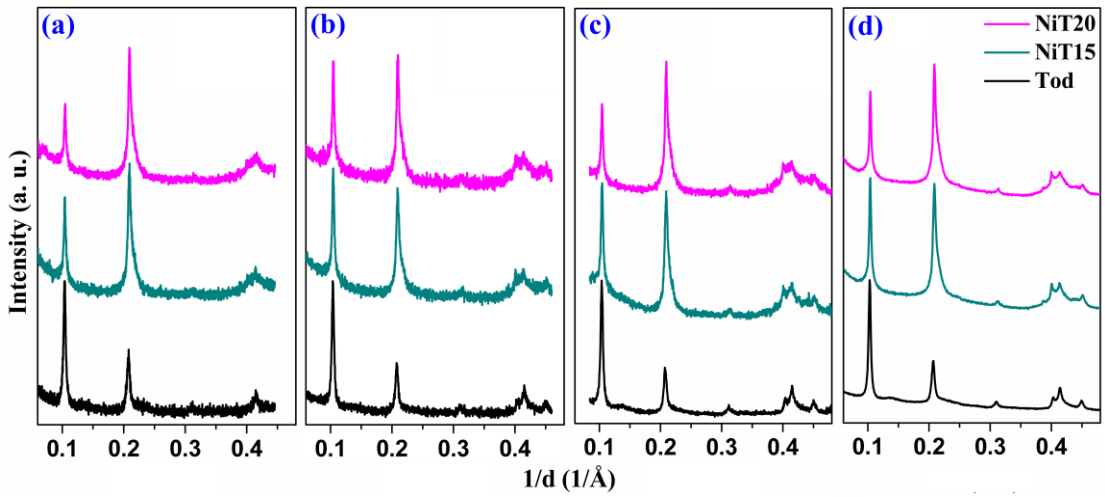


Fig. 1. XRD patterns of layered precursors (top) and reflux products (bottom). Colors correspond to the Ni/(Ni+Mn) ratio of the samples. Green ticks at the bottom of upper and lower figures indicate the reflections of triclinic birnessite (ICDD #43-1456) and todorokite (ICDD #38-0475), respectively.



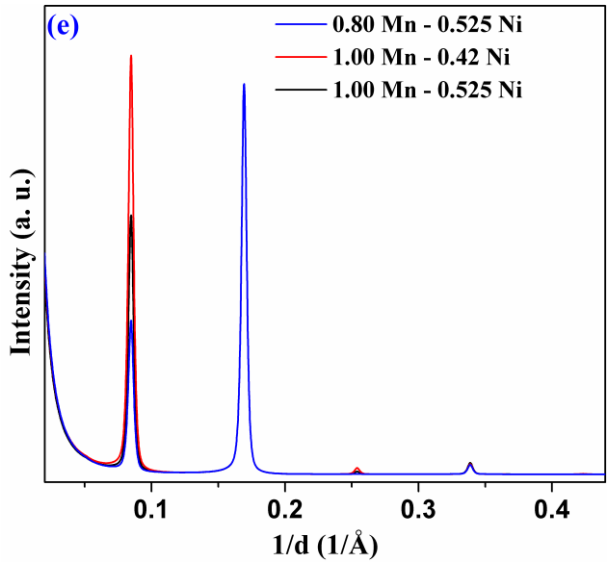


Fig. 2. XRD patterns collected for NiT20, NiT15, and Tod at (a) Mn K-edge (6.5 keV), (b) Ni K-edge (8.3 eV), (c) 12.0 keV, and (d) 18.0 keV. Intensities were systematically normalized to the most intense reflection. Colors as in Fig. 1. (e) XRD patterns calculated for an asbolane containing 0.525 $Ni(OH)_2$ in MnO_2 interlayers. Contents of Ni and Mn atoms are reduced by 20% at their respective absorption edges to simulate the anomalous effect.

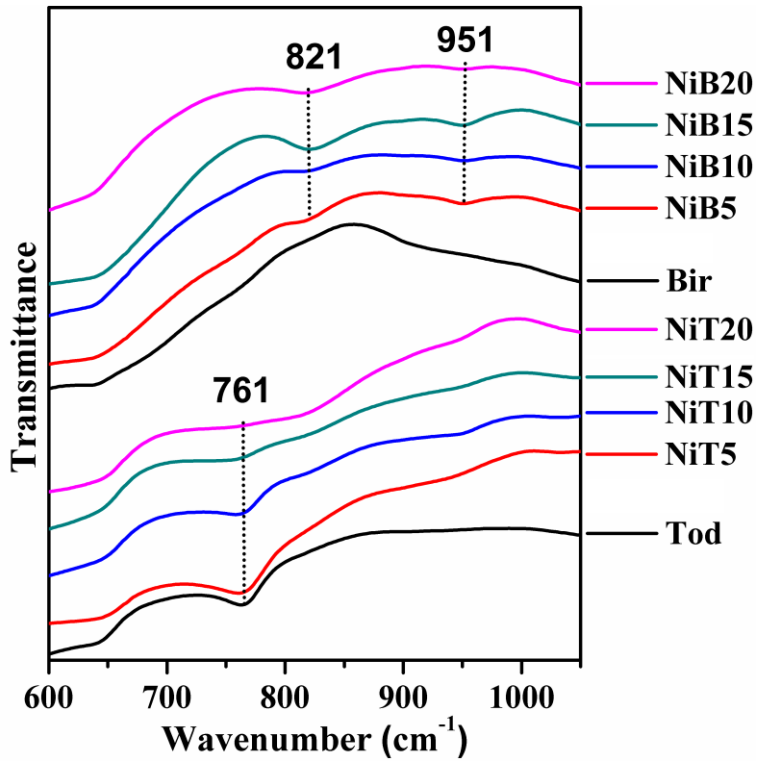


Fig. 3. FTIR spectra of layered precursors and reflux products (top and bottom, respectively). Colors as in Fig. 1.

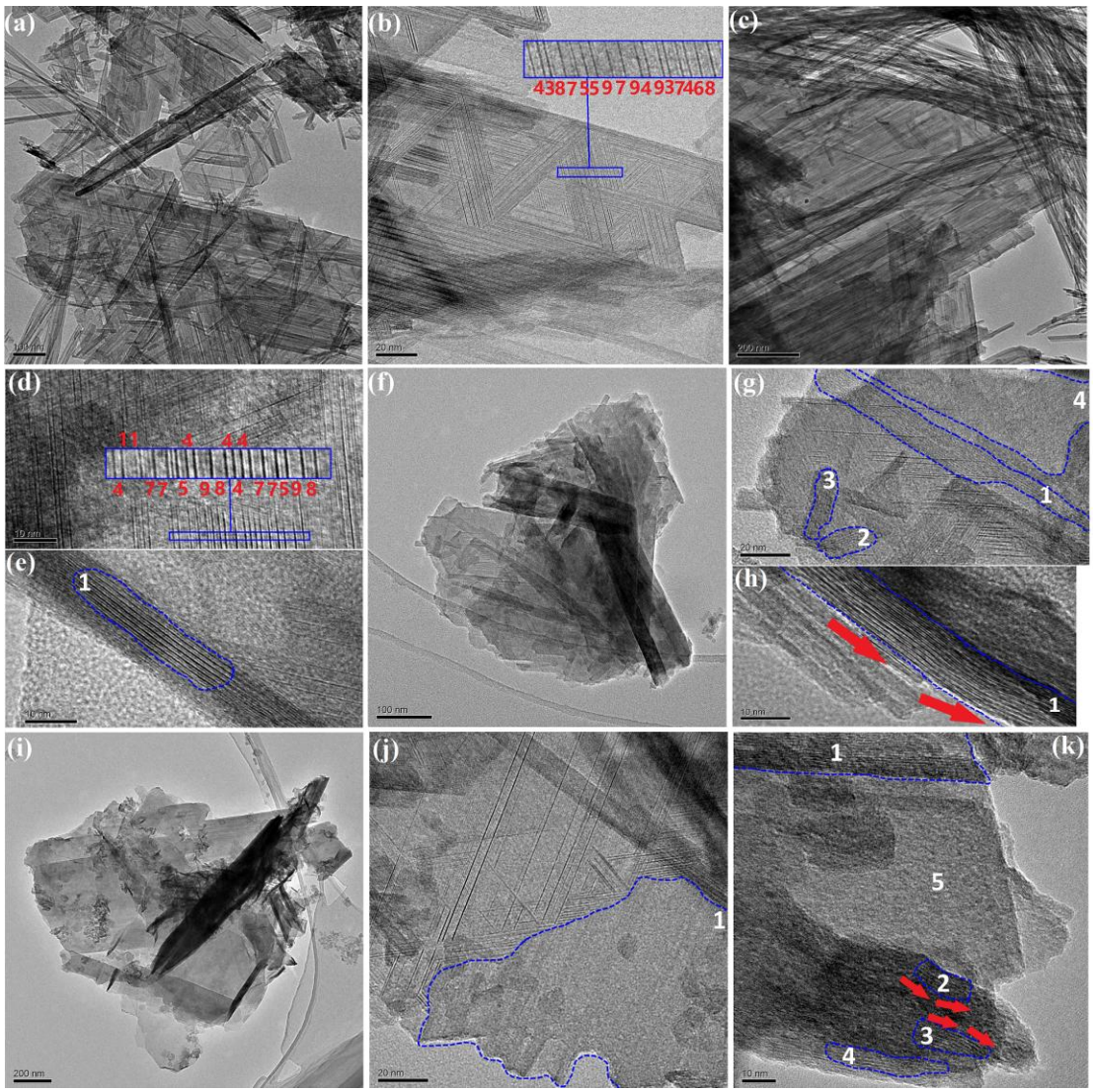


Fig. 4. HRTEM images of (a-b): Tod, (c-e): NiT1, (f-h): NiT5, (i-m): NiT1. Numbers in (b) and (d) indicate the number of MnO_6 octahedra defining tunnel width. Arrows in (i) and (l) indicate the direction of fringes bending.

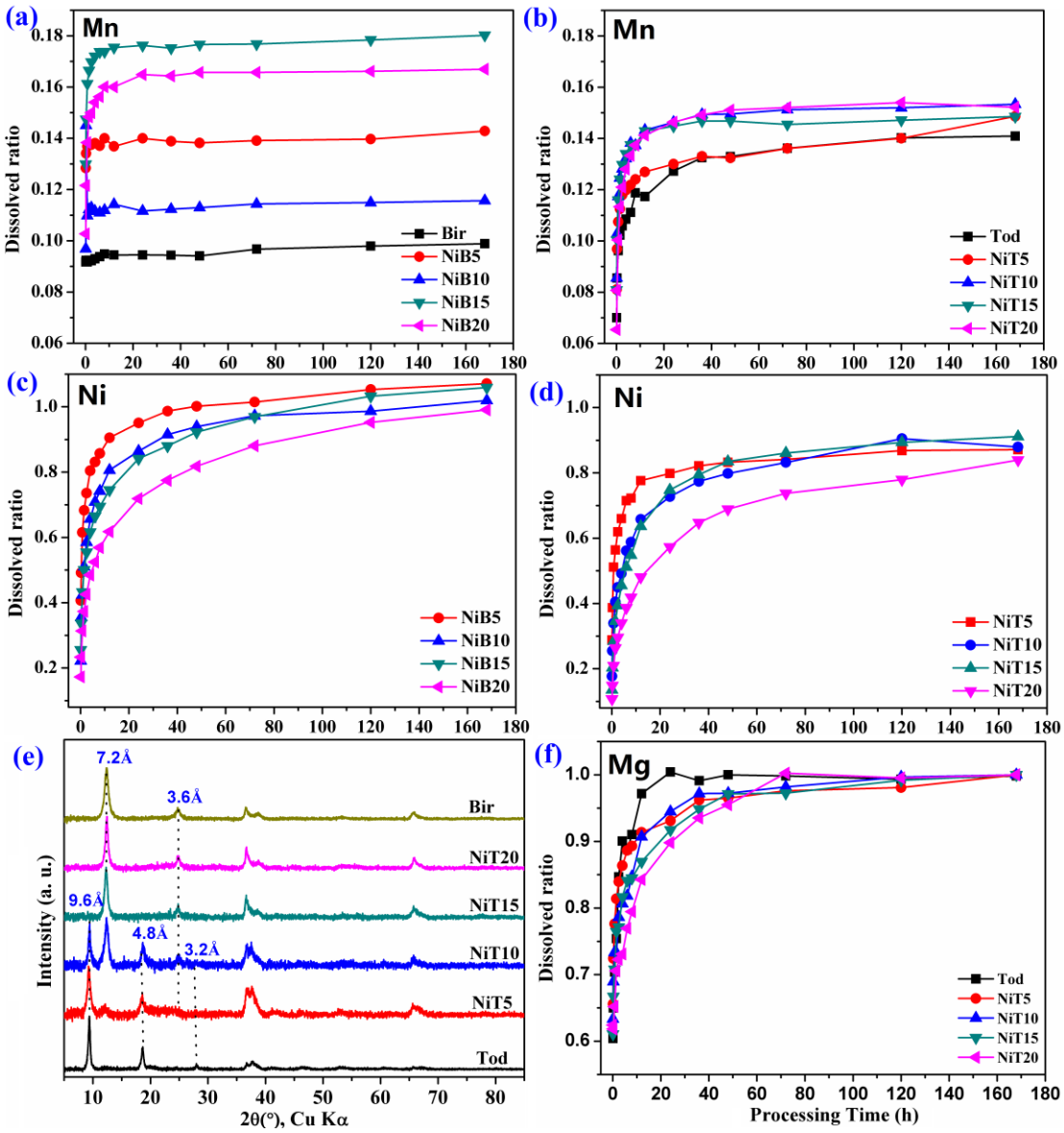


Fig. 5. Proportion of metal cations released during the nitric acid treatment: (a-b): Mn, (c-d): Ni, and (f): Mg. The amount of metal released is normalized to the sample overall metal content (see text for details). (e): XRD patterns of samples treated with nitric acid. Colors as in Fig. 1 except for Bir in (e).

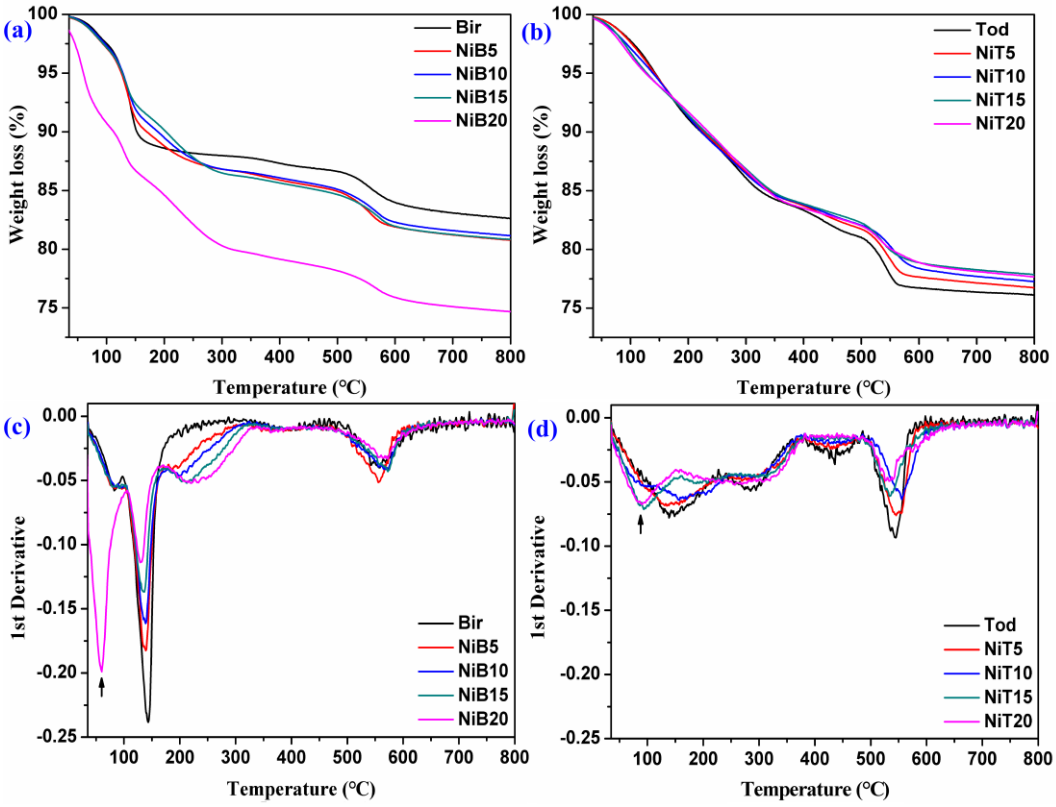


Fig. 6. Thermogravimetric analysis traces obtained for (a) layered precursors and (b) reflux products, and their 1st derivatives (c and d, respectively). 1st derivative curves were smoothed using a Savitzky-Golay filter and a 15 points window. Colors as in Fig. 1.

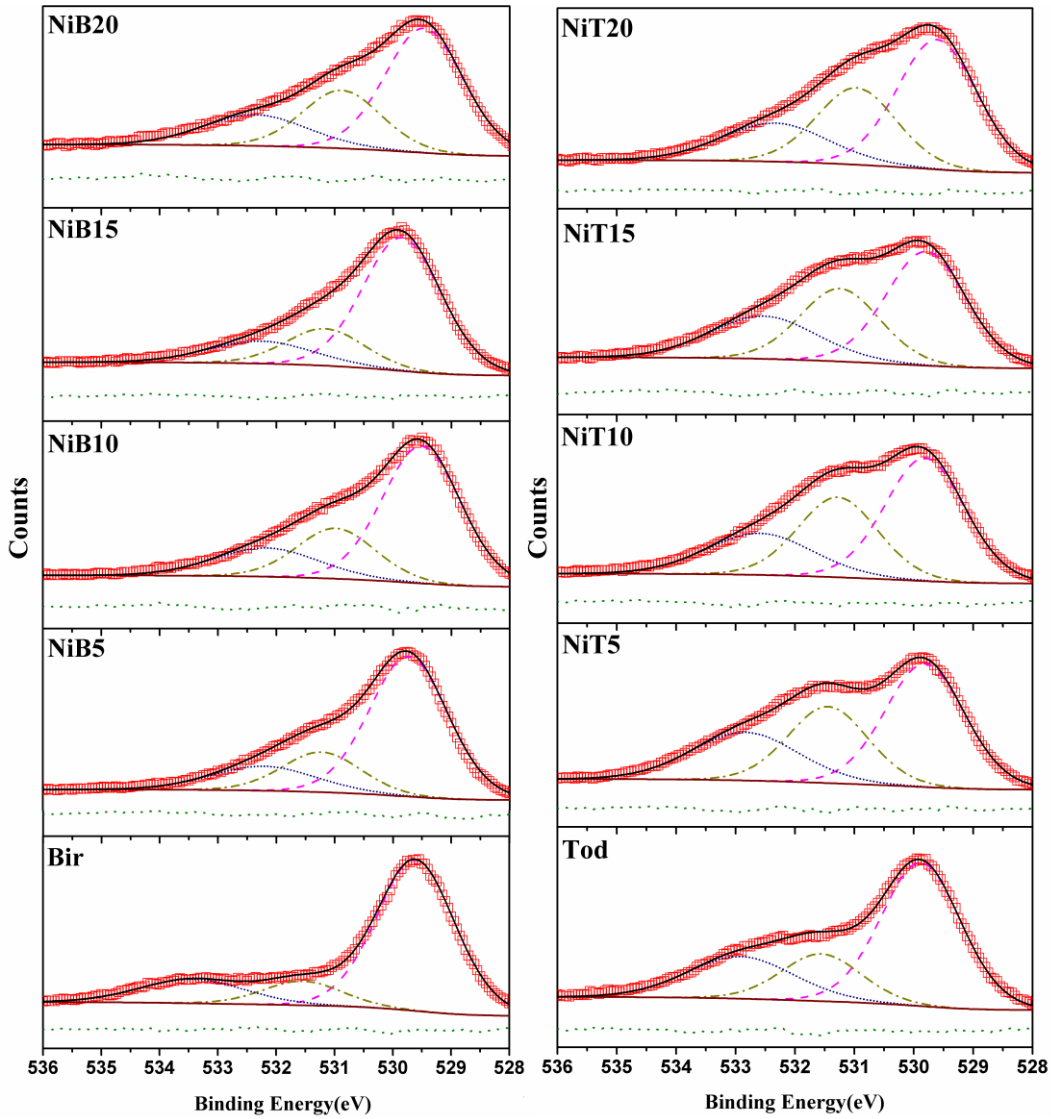


Fig. 7. XPS O1s spectra obtained for layered precursors and reflux products (left and right, respectively). The thick solid curve represents the best fit to the data (open red squares). Peaks corresponding to O^{2-}, OH^{-}, and H_2O species are shown in the order of increasing binding energy as dashed purple, dotted-dashed green, and dotted blue lines, respectively. The green dotted line is the difference curve.

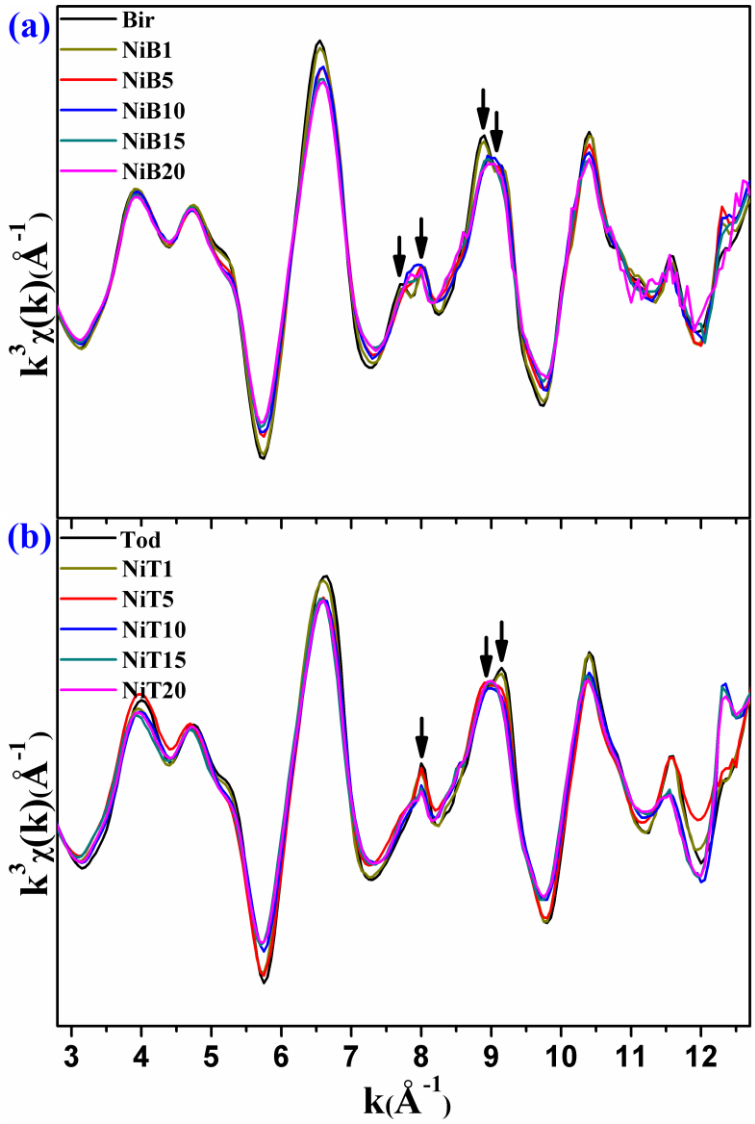


Fig. 8. Mn K-edge EXAFS spectra obtained for (a) layered precursors and (b) reflux products. Colors as in Fig. 1.

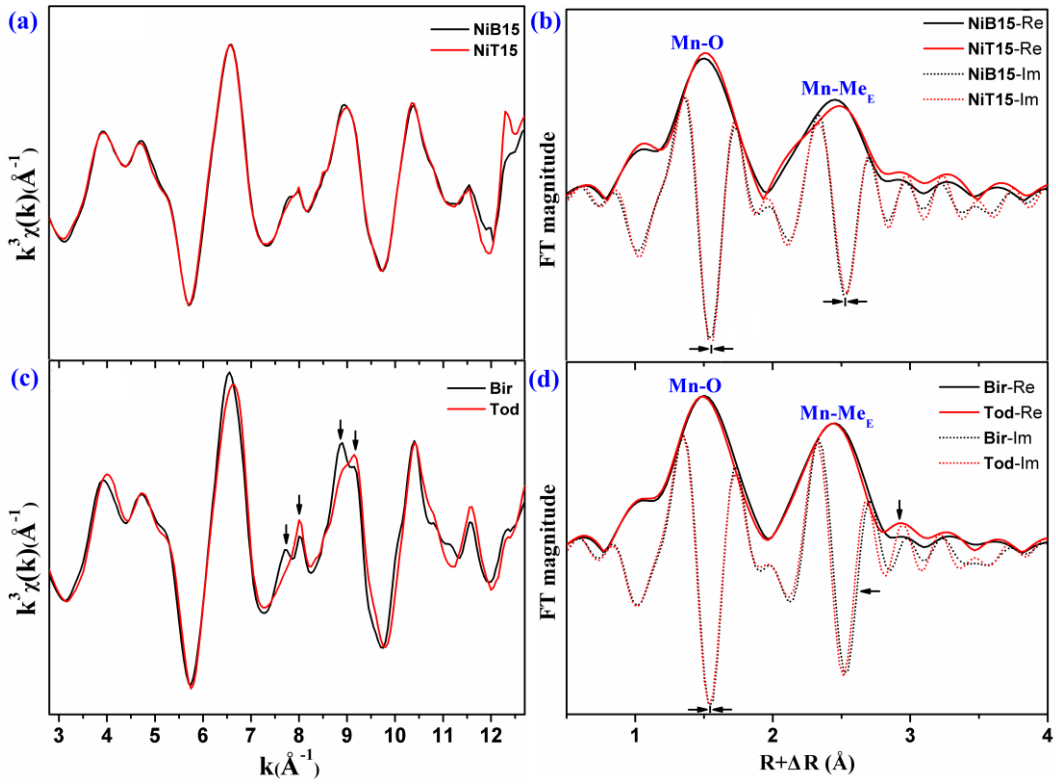


Fig. 9. Comparison of (a, c) Mn K-edge EXAFS and (b, d) of their FTs (showing both real and imaginary parts) obtained for Ni-rich (Top: NiB15 and NiT15) and Ni-free (bottom: Bir and Tod) layered precursors and corresponding reflux products.

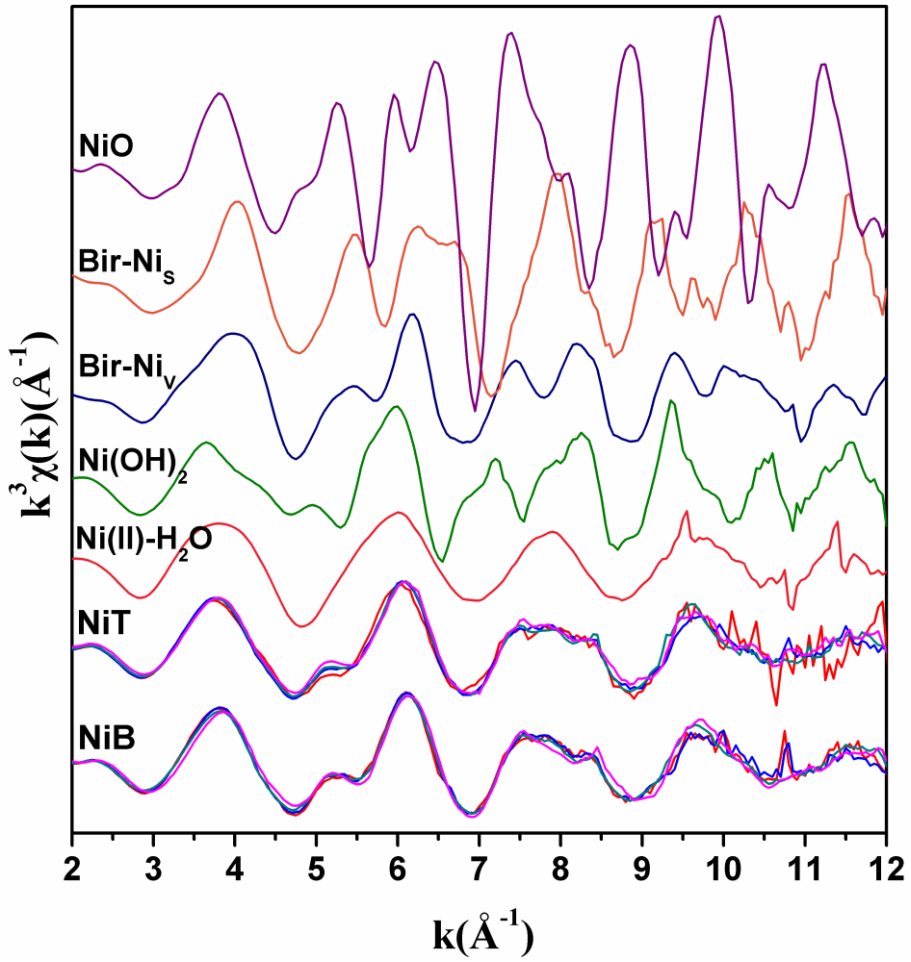


Fig. 10. Comparison of Ni K-edge EXAFS spectra obtained for layered precursors and reflux products with reference spectra. Sample colors as in Fig. 1.

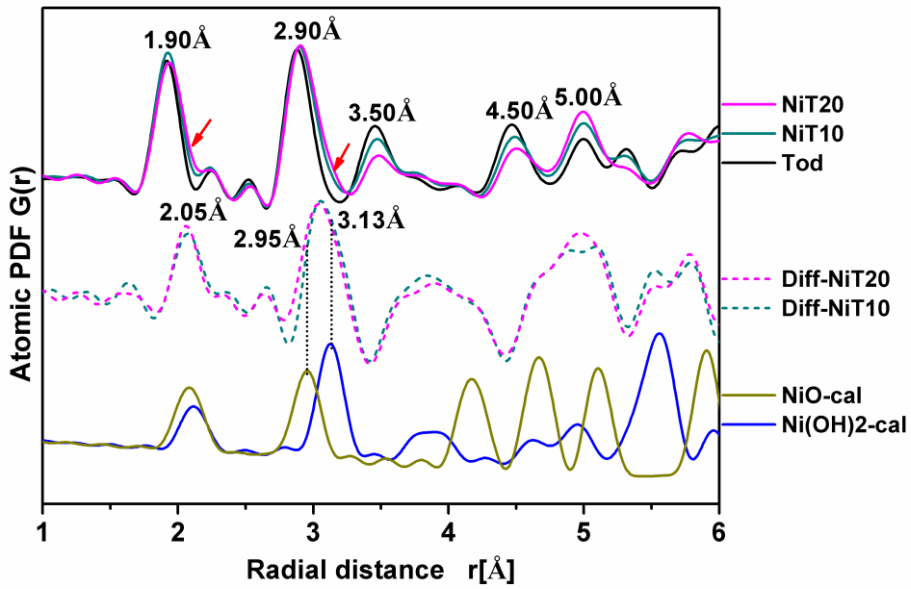


Fig. 11. Pair distribution functions obtained for Ni-rich (NiT10 and NiT20) and

Ni-free (Tod) reflux products (top). Middle: d-PDFs relative to Tod PDF data; bottom: PDFs calculated for Ni (hydr)oxides (ICSD #76670 and #28101 for NiO and $Ni(OH)_2$, respectively). Intensities of experimental PDFs and of difference PDFs were normalized to the 2.9-3.1 Å peak.

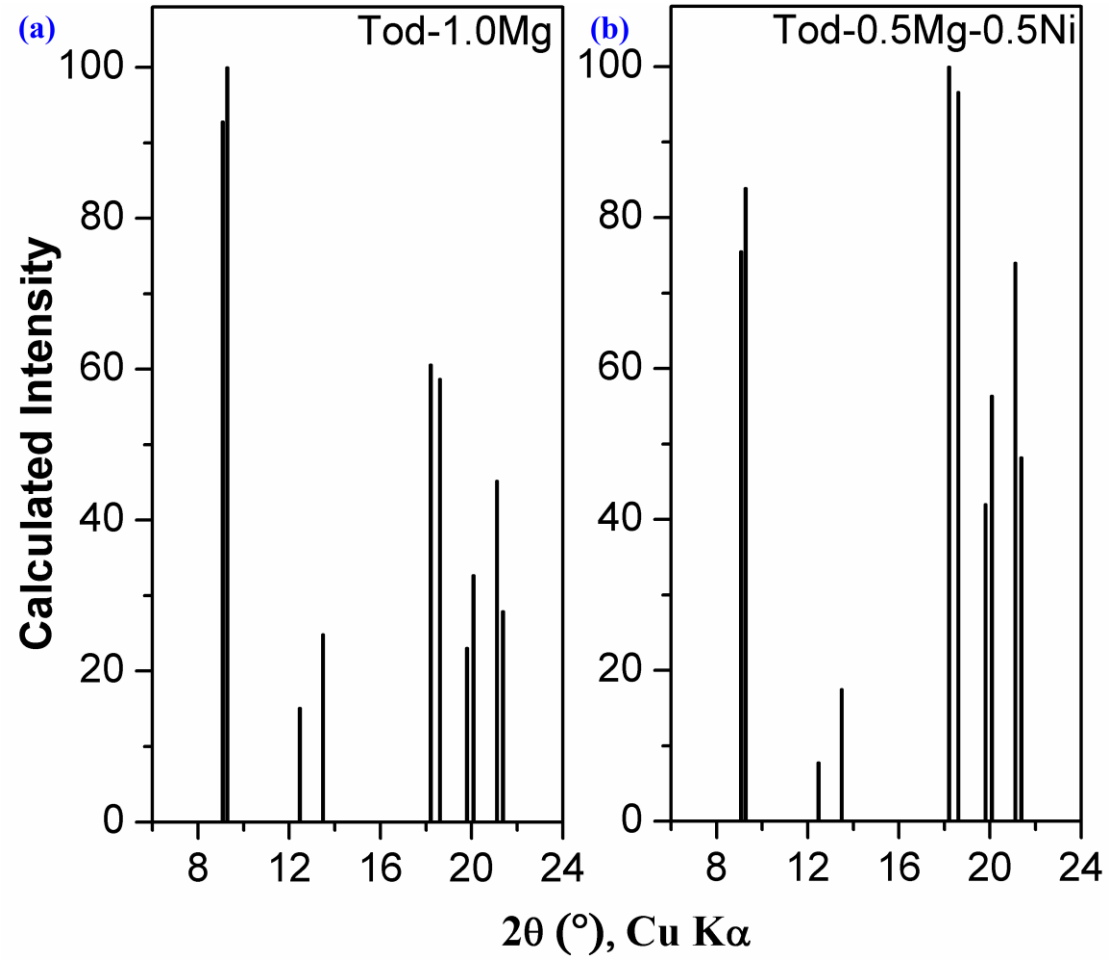


Fig. 12. Intensity distributions calculated for ideal todorokite (ICDD #38-0475) with (a) only Mg in todorokite tunnels and (b) with Mg and Ni present in a 1:1 ratio in todorokite tunnels. In both cases, the model of Post et al.(2003) was modified assuming the complete filling of the O8 site by H_2O molecules (no cations) and the presence of 1.0 cation (Mg or Mg+Ni) in the Mg site.

Transformation of Ni-containing birnessite to tectomanganate: Influence and fate of weakly bound Ni(II) species

Supplementary material

Geochimica Et Cosmochimica Acta

Zhongkuan Wu[a,b], Bruno Lanson[b,*], Xionghan Feng[a], Hui Yin[a], Zhangjie Qin[a], Xiaoming Wang[a], Wenfeng Tan[a], Zhongjun Chen[c], Wen Wen[d], Fan Liu[a,*]

[a] *Key Laboratory of Arable Land Conservation (Middle and Lower Reaches of Yangtse River) Ministry of Agriculture, College of Resources and Environment, Huazhong Agricultural University, Wuhan 430070, China*

[b] *Univ. Grenoble Alpes, Univ. Savoie Mont Blanc, CNRS, IRD, IFSTTAR, ISTerre, F-38000 Grenoble, France*

[c] *Beijing Synchrotron Radiation Facility, Institute of High Energy Physics, Chinese Academy of Sciences, Beijing 100039, China*

[d] *Shanghai Synchrotron Radiation Facility, Shanghai Advanced Research Institute Chinese Academy of Sciences, Shanghai 201204, China*

** Corresponding author: bruno.lanson@univ-grenoble-alpes.fr; liufan@mail.hzau.edu.cn*

Table S1

Relative proportions of O species in the near-surface of layered precursors and reflux products calculated by fitting XPS O1s data

Sample	O1s (BE)	State	BE(eV)	FWHM(eV)	At.%
Bir	529.35	O^{2-}	529.6	1.59	72.9
		OH^-	531.5	1.59	11.6
		H_2O	533.4	2.12	15.5
NiB5	529.72	O^{2-}	529.7	1.59	65.9
		OH^-	531.2	1.59	18.8
		H_2O	532.2	2.12	15.3
NiB10	529.72	O^{2-}	529.5	1.59	60.8
		OH^-	531.0	1.59	22.3
		H_2O	532.2	2.12	16.9
NiB15	530.06	O^{2-}	529.8	1.59	66.6
		OH^-	531.2	1.59	18.5
		H_2O	532.3	2.12	15.0
NiB20	530.21	O^{2-}	529.5	1.59	55.6
		OH^-	530.9	1.59	25.9
		H_2O	532.4	2.12	18.5
Tod	529.89	O^{2-}	529.9	1.59	58.1
		OH^-	531.6	1.59	20.9
		H_2O	533.0	2.12	21.0
NiT5	529.84	O^{2-}	529.8	1.59	46.7
		OH^-	531.4	1.59	29.0
		H_2O	532.8	2.12	24.4
NiT10	530.08	O^{2-}	529.8	1.59	47.6
		OH^-	531.3	1.59	31.0
		H_2O	532.6	2.12	21.5
NiT15	530.15	O^{2-}	529.8	1.59	46.8

		OH^-	531.2	1.59	28.9
		H_2O	532.5	2.12	23.4
		O^{2-}	529.6	1.59	50.3
NiT20	529.59	OH^-	531.0	1.59	29.8
		H_2O	532.3	2.12	19.9

Table S2

Relative proportions of NiB and $Ni(OH)_2$ species obtained from linear combination fitting of NiT K-edge EXAFS spectra using $Ni(OH)_2$ and corresponding NiB samples as standard references (Fig. S5).

Samples	NiB*n* /%	$Ni(OH)_2$ /%	Error /%
NiT5	82.0	18.0	2.1
NiT10	86.5	13.5	1.0
NiT15	87.1	12.9	0.9
NiT20	85.3	14.7	1.1

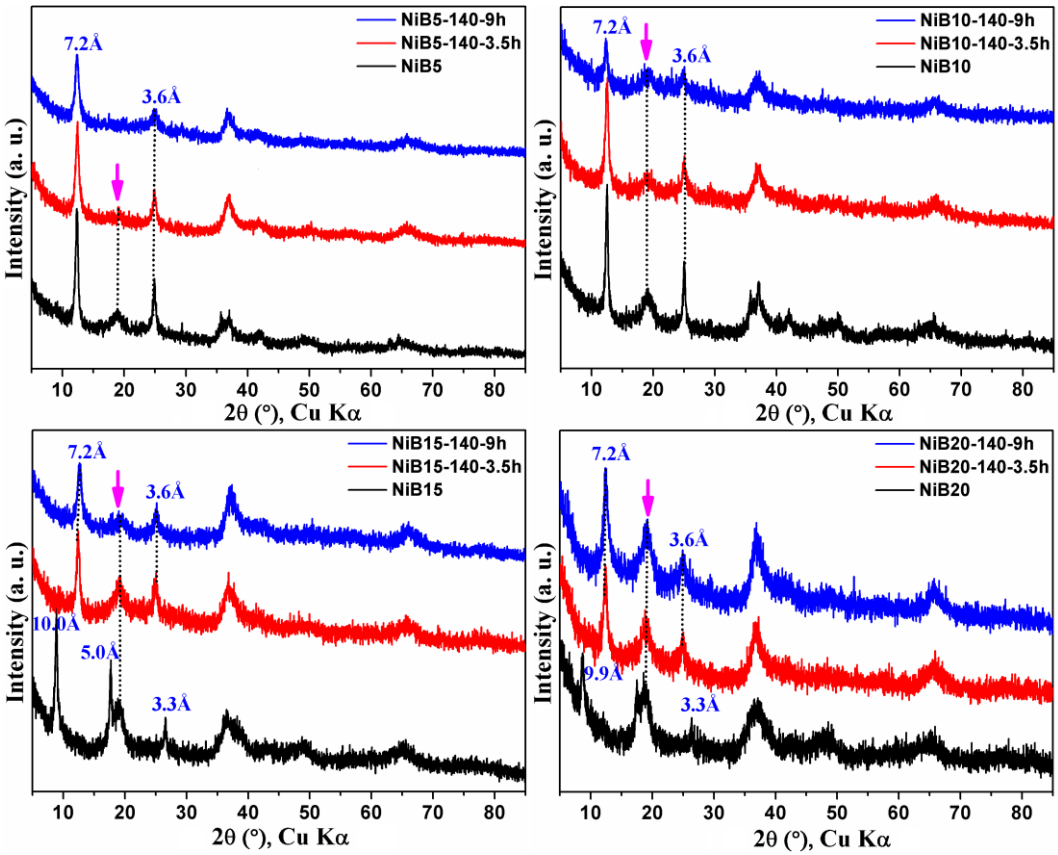


Fig. S1. XRD patterns of fresh layered precursors after heating to 140 °C for different durations

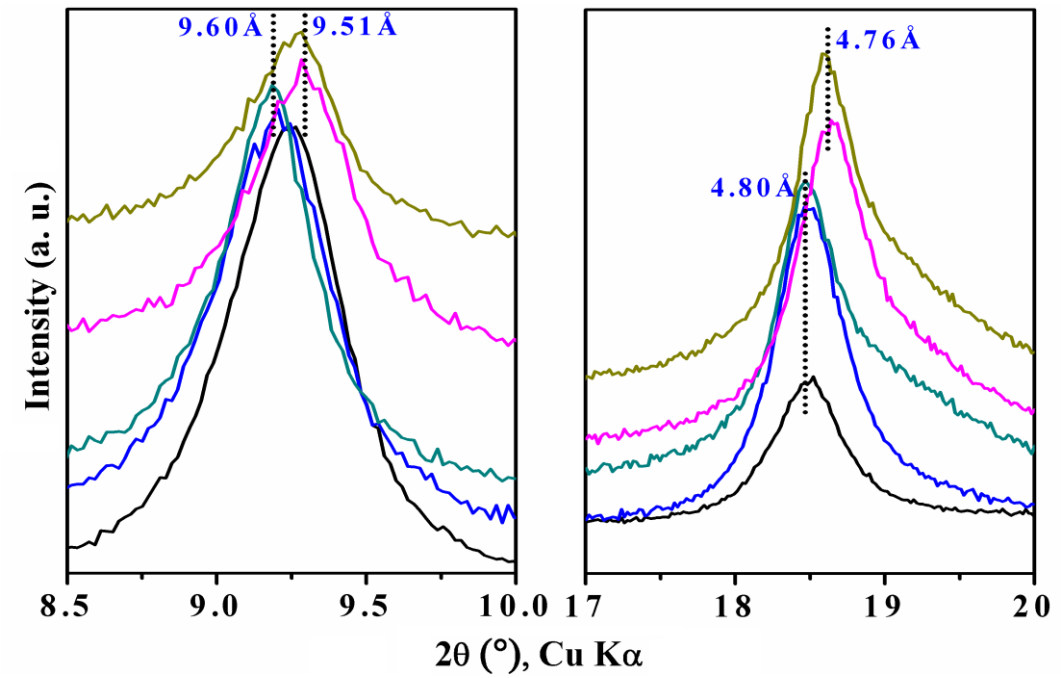


Fig. S2. XRD patterns of reflux products (zoom on low-angle regions). Colors as in Fig. 1.

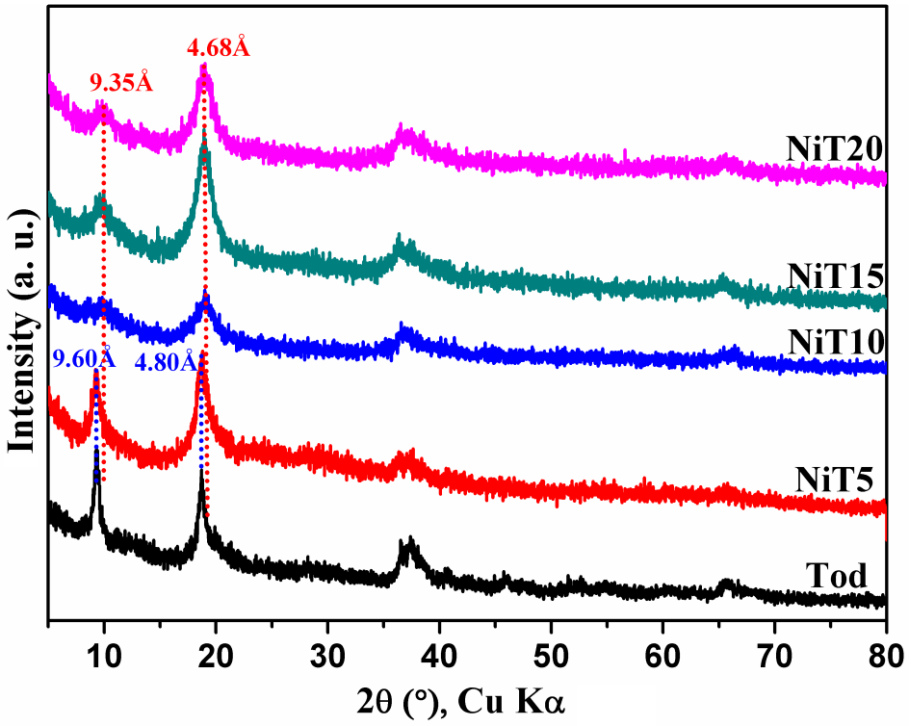


Fig. S3. XRD patterns of reflux products after heating to 140 °C for 12 hours. Colors as in Fig. 1.

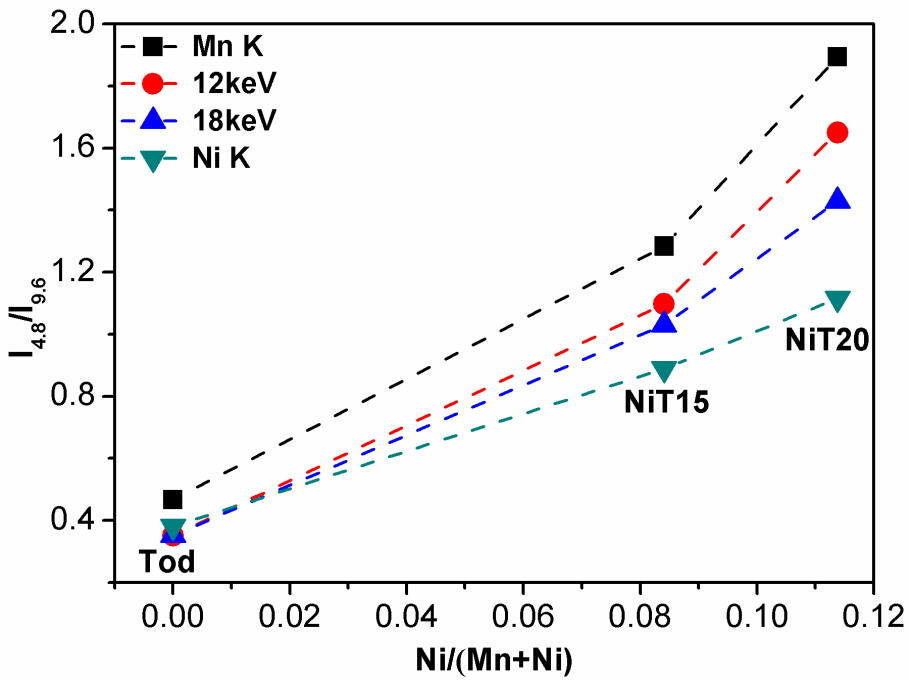


Fig. S4. Intensity ratio of the intensity of 4.8 Å and 9.6 Å peaks ($I_{4.8}/I_{9.6}$) in reflux products as a function of Ni content and X-ray energy (see Fig. 2 for the data).

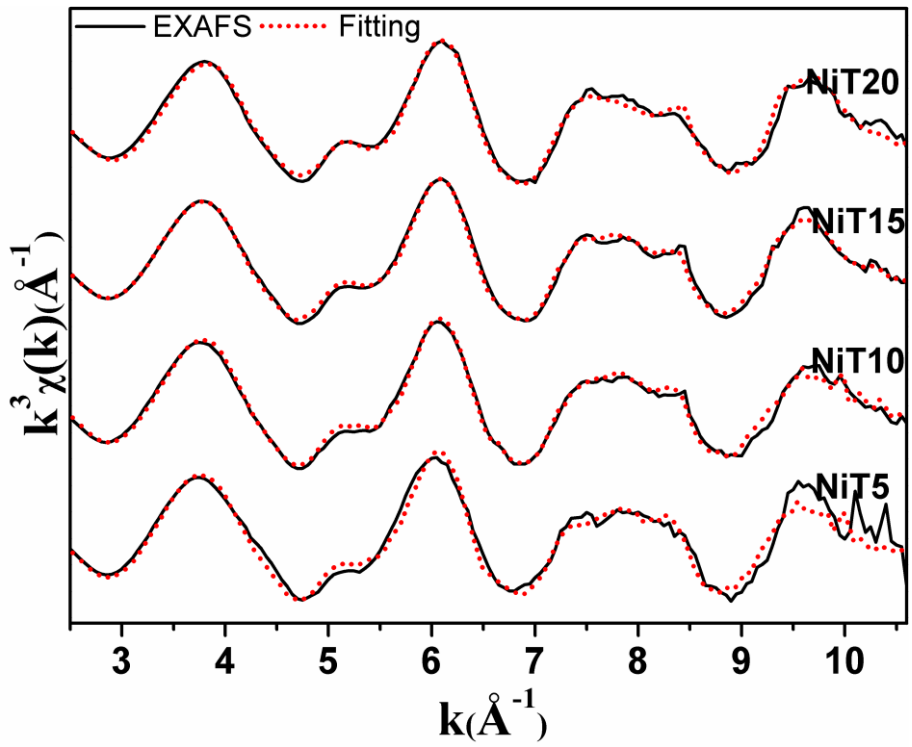


Fig. S5. Linear combination fitting of NiT K-edge EXAFS spectra using $Ni(OH)_2$ and corresponding NiB samples as standard references.

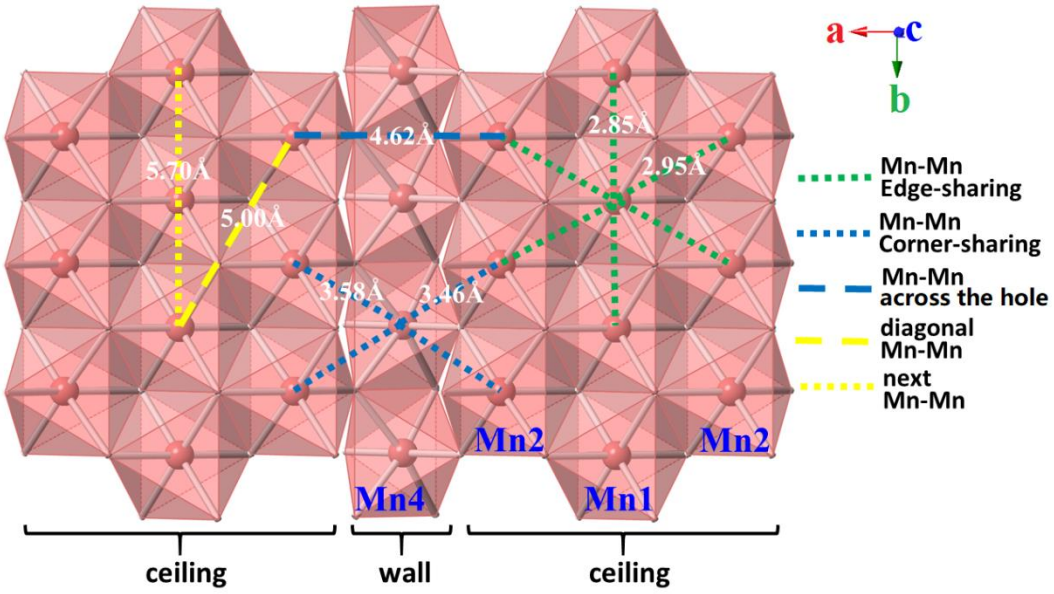


Fig. S6. Interatomic distances calculated for a variety of Mn-Mn pairs and ideal todorokite structure (ICDD #38-0475). The Mn4-Mn4 distance (4.48 Å) which is not reported in the figure is similar to the Mn2-Mn2 distance. Figure modified from Fig. 1(b) in Wu et al. (2019).

REFERENCES

Wu Z., Peacock C.L., Lanson B., Yin H., Zheng L., Chen Z., Tan W., Qiu G., Liu F. and Feng X. (2019) Transformation of Co-containing birnessite to todorokite: Effect of Co on the transformation and implications for Co mobility. *Geochim. Cosmochim. Acta* **246**, 21-40.